Electronic Supplementary Material (ESI) for Chemical Communications.

Supporting Information

Actinide Arene-Metalates: 2. A Neutral Uranium Bis(Anthracenide) Sandwich Complex and Elucidation of its Electronic Structure

Jesse Murillo,[†] Rina Bhowmick,[‡] Katie L. M. Harriman,[‖] Alejandra Gomez-Torres,[†] Joshua Wright,[¥] Pere Miró,[‡] Alejandro Metta-Magana,[†] Muralee Murugesu,[‖] Bess Vlaisavljevich,*[,‡] and Skye Fortier*[,†]

[†]Department of Chemistry and Biochemistry, University of Texas at El Paso, El Paso, Texas 79968, United States

‡Department of Chemistry, University of South Dakota, Vermillion, South Dakota 57069, United States

[‖]Department of Chemistry and Biomolecular Sciences, University of Ottawa, Ottawa, Ontario K1N 6N5, Canada

[¥] Department of Physics, Illinois Institute of Technology, Chicago, Illinois, 60616, United States

*To whom correspondence should be addressed. Email: asfortier@utep.edu, bess.vlaisavljevich@usd.edu

`

Table of Contents

General Considerations. All air and moisture-sensitive operations were performed in either an MBraun glovebox under an atmosphere of ultra-high purity nitrogen or in a Vacuum Atmospheres glovebox under an atmosphere of ultra-high purity argon. Diethyl ether, hexanes, and THF were dried using a Pure Process Technology Solvent Purification System and subsequently stored under an inert atmosphere of argon or nitrogen over activated 4 Å molecular sieves. Pyridine-d_5 (py-d_5) and THF-d_8 were purchased from Cambridge Isotope Laboratories Inc., degassed by three freeze-pump-thaw cycles, and dried over activated 4 Å molecular sieves for at least 24 h prior to use. Hexamethylphosphoramide (HMPA) was distilled over calcium hydride and stored under an inert atmosphere of argon or nitrogen on 4 Å molecular sieves for several days before use. Celite and 4 Å molecular sieves were heated under dynamic vacuum to 150 °C for at least 24 h and then cooled under vacuum. $UI_3(dioxane)_{1.5}$,[1] UCl_4,[2] $U(O)[N(SiMe_3)_2]_3$,[3] $UO_2Cl_2(THF)_3$[4] were synthesized following reported procedures. Anthracene was purchased from Alfa Aesar and used as received. Grade ZG ultra-high purity boron nitride powder with an average particle size of 7.4 μm was purchased from Amazon.com, Inc. and heated under high vacuum at 200 ˚C for several days and subsequently stored in a glovebox under an inert atmosphere of argon prior to use. All other reagents were purchased from commercial suppliers and used as received. Low temperature EPR measurements were performed on a Bruker EMX Plus X-band spectrometer using a liquid helium cooled cryo-stat. ^{1}H NMR spectra were recorded on a Bruker AVANCE III 400 MHz spectrometer. ^{1}H NMR spectra are referenced to residual ^{1}H solvent peaks as internal standards or the characteristic ^{1}H resonances of the solvent. ^{31}P{^{1}H} NMR spectra were referenced to external 85% H_3PO_4. Elemental analyses were performed by Midwest Microlab, LLC and ALS Group USA, Corp. UV-vis/NIR spectra were recorded on a Cary 5000 spectrophotometer in airtight, match-paired UV-vis cuvettes.

X-ray absorption near edge structure (XANES). All X-ray absorption experiments were conducted at sector 10-BM of the Advanced Photon Source at Argonne National Laboratories, currently of the Materials Research Collaborative Access Team (MRCAT).[5] Data was collected in the standard transmission geometry mode with an incident beam of 500 × 1000 μm @ 10^{12} ph/sec with energies between 17 – 18 keV. All sample energies are referenced to an yttrium foil located between the second and third detectors, and all spectra are aligned to a foil value of 17038.4 eV (Figure S13). Under an inert atmosphere of high purity argon, sample powders were prepared by mixing boron nitride powder with the uranium compounds to concentrations between 20 – 40

wt. % in the analyte and ground using a mortar and pestle to produce ~0.1 g of a very fine powder. Approximately 0.06 g of the powder was loaded into a pellet press and compressed using a force not exceeding 27 Newton-meters to produce a pellet 7 mm in diameter and 1 – 2 mm in depth. The pellet was then carefully sandwiched between two polypropylene plastic disks for structural support and sealed between two layers of Kapton tape. The pellet assembly was again wrapped in another layer of Kapton, and the package then vacuum sealed inside of a 3 × 3 cm ethylene-vinyl acetate (EVA) pouch. As required by the beamline radiation safety protocols, the seams of the EVA pouch were reinforced with Kapton tape. The integrity of the vacuum seal was monitored over several days and closely reexamined immediately prior to the data collection. The compounds $UI_3(dioxane)_{1.5}$, UCl_4, $U(O)[N(SiMe_3)_2]_3$, and $UO_2Cl_2(THF)_3$ were used as oxidation state reference standards for U(III), U(IV), U(V), and U(VI), respectively.

Each uranium sample was prepared and measured in duplicate. Presented data was produced as an average of three consecutive scans for each sample. All data was processed and figures generated using *Demeter* X-ray absorption spectroscopy data analysis software.[6] The edge energies are determined as the inflection point of the first derivative as calculated by the *Demeter* software program. The white line energies are defined as the peak absorption maxima as identified through the *Demeter* program.

Magnetic Measurements. The magnetic susceptibility measurements were obtained using a Quantum Design SQUID magnetometer MPMS-XL7 operating between 1.8 and 300 K. DC measurements were performed on a polycrystalline sample of **1**·THF. The samples were restrained with silicon grease and wrapped in a polyethylene membrane under an inert atmosphere. The samples were subjected to DC fields of -7 to 7 T, and a 3.78 Oe driving field was used for AC measurements. The magnetization data were collected at 100 K to check for ferromagnetic impurities that were absent in both samples. Diamagnetic corrections were applied for the sample holder and the inherent diamagnetism of the samples were estimated with the use of Pascals constants.

X-ray Crystallography. Data for **2**, **1**·THF and **3**·THF·C_6H_{14} were collected on a dual source Bruker D8 4-axis diffractometer equipped with a PHOTON II CPAD detector with a IμS Mo Kα X-ray source (α = 0.71073 Å) fitted with a HELIOS MX monochromator. The crystals were mounted on a Mitigen Kapton loop coated in NVH oil and maintained at 100(2) K under a flow of nitrogen gas during data collection. Data collection and cell parameter determination were

conducted using the SMART[7] program. Integration of the data and final cell parameter refinements were performed using SAINT[8] software with data absorption correction implemented through SADABS.[9] Structures were solved using intrinsic phasing methods and difference Fourier techniques. All hydrogen atom positions were idealized and rode on the atom of attachment. Structure solution, refinement, graphics, and creation of publication materials were performed using SHELXTL[10] or the Olex2[11] crystallographic package.

In **2**, there is positional disorder present on one of the methyl groups of a phosphoramide substituent which has been modeled by the use of SIMU restraints on C4/N1/C3 and ISOR on C6. Additionally, **2** crystallizes as a racemic twin and an inversion matrix (-1 0 0 0 -1 0 -1 0 0) has been applied within Olex2 accordingly.

Complete crystallographic data has been deposited at the Cambridge Crystallographic Data Center (CCDC Nos. 2172190 (**1**·THF), 2172188 (**2**), 2172189 (**3**·THF·C_6H_{14})).

Synthesis of [UI_2(HMPA)$_4$]I (**2**). To a 20 mL scintillation vial, 214.2 mg (0.29 mmol) of UI_3(dioxane)$_{1.5}$ was suspended in THF (8 mL). To this, while stirring at room temperature, 0.2 mL (1.14 mmol) of HMPA was added via a micropipette. The solution changed from blue to dark purple accompanied by the formation of a dark precipitate. The reaction was stirred at room temperature for 4 h. The resulting dark purple suspension was filtered via a medium-porosity glass frit. The dark purple solid collected on the frit was washed with THF (30 mL). The dark solid was then dried under vacuum for 1 h. Yield: 394.3 mg (0.268 mmol), 94%. **2** is sparingly soluble in THF to give a deep purple solution, which upon storage at -35 °C for 24 h, gives dark purple plate shaped crystals of X-ray quality. ^{1}H NMR (25 °C, 400 MHz, py-d_5): δ 1.57 (br s, 3H, -N*Me*), 2.54 (br s, 9H, -N*Me*), 9.48 (br s, 48H, -N*Me*), 10.07 (br s, 6H, -N*Me*), 13.10 (br s, 6H, -N*Me*). ^{31}P{^{1}H} NMR (25 °C, 162 MHz, py-d_5): δ 24.60 (s). UV–vis (pyridine, 25 °C, nm, arbitrary units): 338 (0.22), 358 (0.14), 392 (0.10), 486 (0.22), 587 (0.13). Anal. Calcd for **2**, $C_{24}H_{72}O_4N_{12}P_4I_3U$: C, 21.58; H, 5.43; N, 12.59. Found: C, 22.42; H, 5.47; N, 12.06. (Note: Multiple combustion analyses attempts failed to give satisfactory results for carbon.)

Synthesis of [U(η^6-$C_{14}H_{10}$)(η^4-$C_{14}H_{10}$)(HMPA)$_2$]·THF (**1**·THF**)**. To a 20 mL scintillation vial, 8.4 mg (0.22 mmol) of potassium metal was suspended in THF (5 mL). To this, while stirring at room temperature, 37.3 mg (0.21 mmol) of anthracene was added, forming a dark blue solution. The reaction was left to stir at room temperature until all potassium metal was consumed, leaving

a deep blue solution. The blue solution was chilled to -35 °C, then 105.2 mg (0.07 mmol) of **2** was added and the reaction mixture was left to stir at -35 °C for 14 h. The resulting purple/white suspension was filtered through Celite supported on a medium-porosity glass frit. The dark purple filtrate was layered with hexanes (1:1 with THF) and the mixture was stored at -35 °C. After 24 h, dark purple, block shaped, X-ray quality crystals were formed. Yield: 50.1 mg (0.049 mmol), 65%. ^{1}H NMR (25 °C, 400 MHz, THF-d_8): δ 2.56 (s, -NMe_2, integration value exceeds that expected for 2 coordinated HMPA ligands), 12.63 (br s, 8H, $C_{14}H_{10}$), -46.02 (br s, 12H, $C_{14}H_{10}$). ^{31}P{^{1}H} NMR (25 °C, 162 MHz, THF-d_8): δ 87.16 (s). UV–vis (THF, 25 °C, nm, arbitrary units): 312 (0.7), 326 (0.9), 340 (1.3), 358 (1.7), 377 (1.5). Anal. Calcd for **1**·THF, $C_{44}H_{64}O_3N_6P_2U$: C, 51.56; H, 6.29; N, 8.20. Anal. Calcd for **1**, $C_{40}H_{56}O_2N_6P_2U$: C, 50.42; H, 5.92; N, 8.82. Found: C, 45.80; N 5.91; N, 8.45. (Note: Combustion analyses of several independently prepared samples failed to give satisfactory results. This may be due to the high air sensitivity of the complex.)

Synthesis of [U(η^6-$C_{14}H_{10}$)(η^6-$C_{14}H_{10}$)(HMPA)(THF)]·THF·C_6H_{14} (3·THF·C_6H_{14}**).** To a 20 mL scintillation vial, 45.0 mg (43.9 μmol) of **1**·THF was dissolved in 4 mL of THF. The dark purple suspension was chilled to -35 °C, then 11.8 mg (45.9 μmol) of AgOTf was added, making a dark red solution. This reaction was left to stir at -35 °C for 1 h, then the resulting red solution was filtered through Celite supported on a medium-porosity glass frit. The crimson red filtrate was layered with hexanes (1:1 with THF), and the mixture was stored at -35 °C. After 3 d, dark red/burgundy X-ray quality crystals in the shape of blocks were formed. Yield: 28.0 mg (30.0 μmol), 68%. (Note: All attempts to repeat the synthesis of **3** were unsuccessful, producing **1** as the only tractable product.)

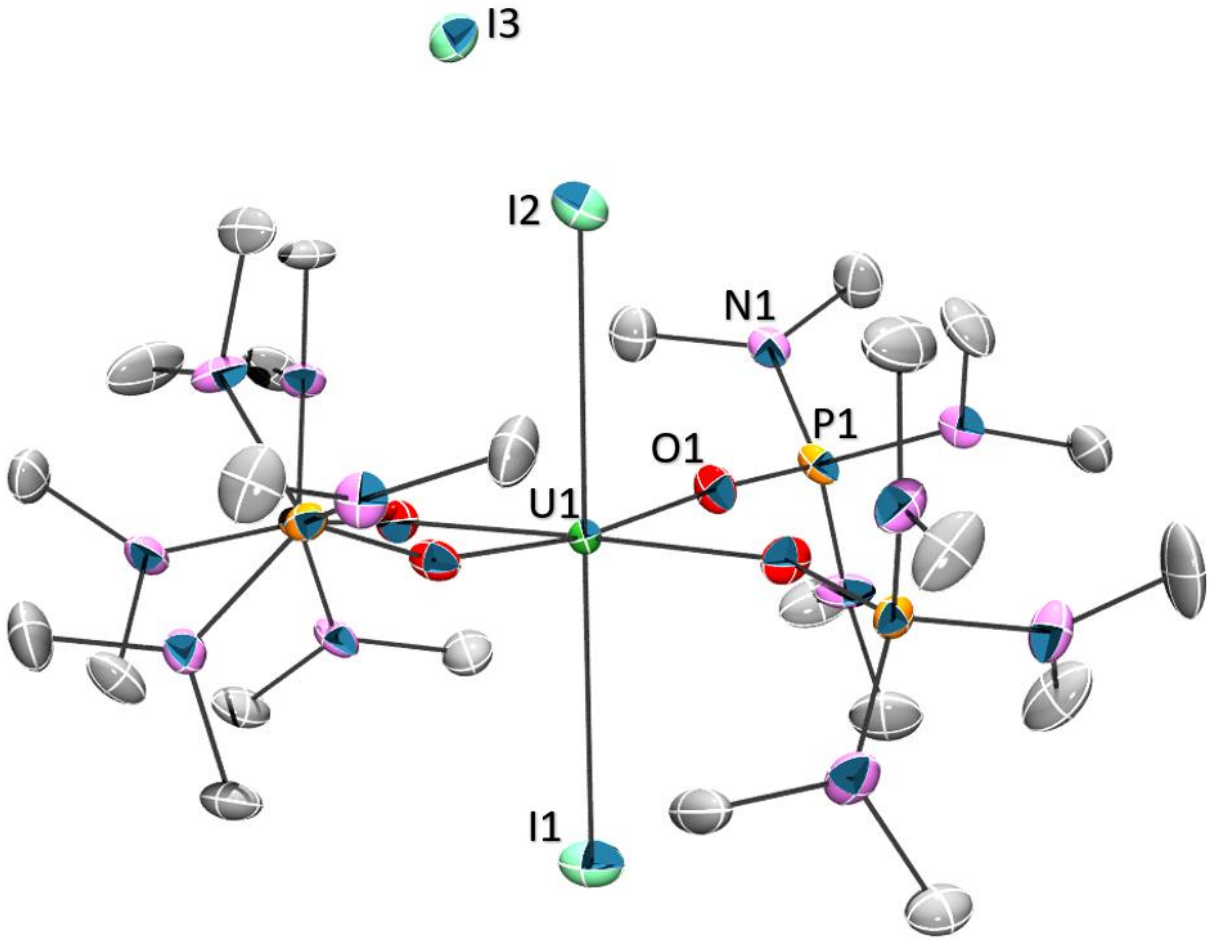

Figure S1. ORTEP diagram of **2** with 30% probability thermal ellipsoids. Only one molecule of two located in the asymmetric unit is shown. Hydrogen atoms are omitted for clarity.

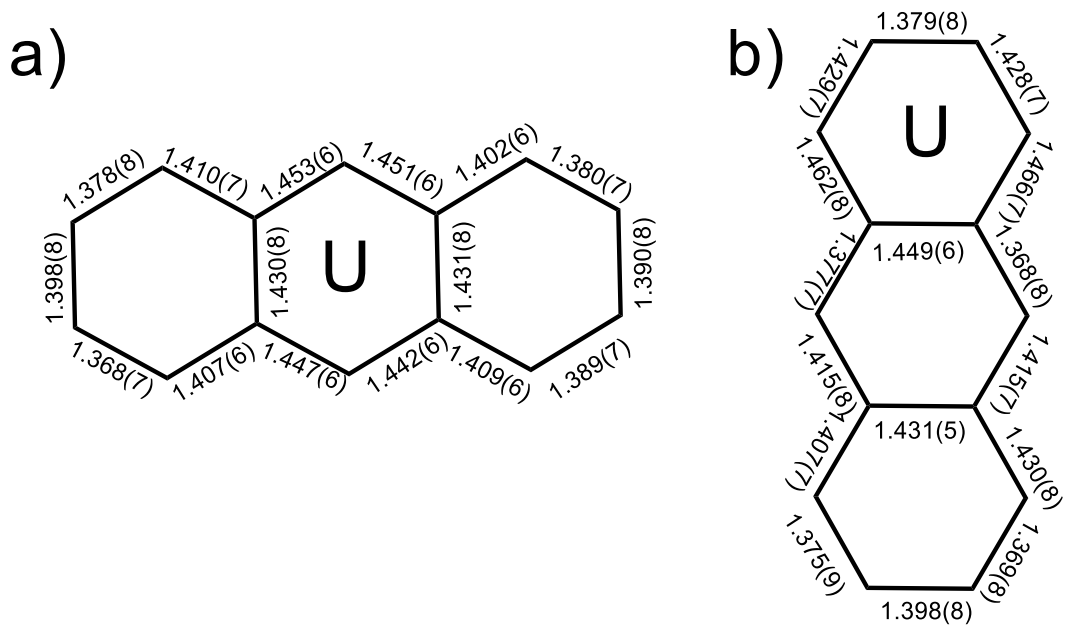

Figure S2. Carbon-carbon bond length diagrams in **1**·THF for the a) η^6-coordinated anthracenide and b) η^4-coordinated anthracenide ligands.

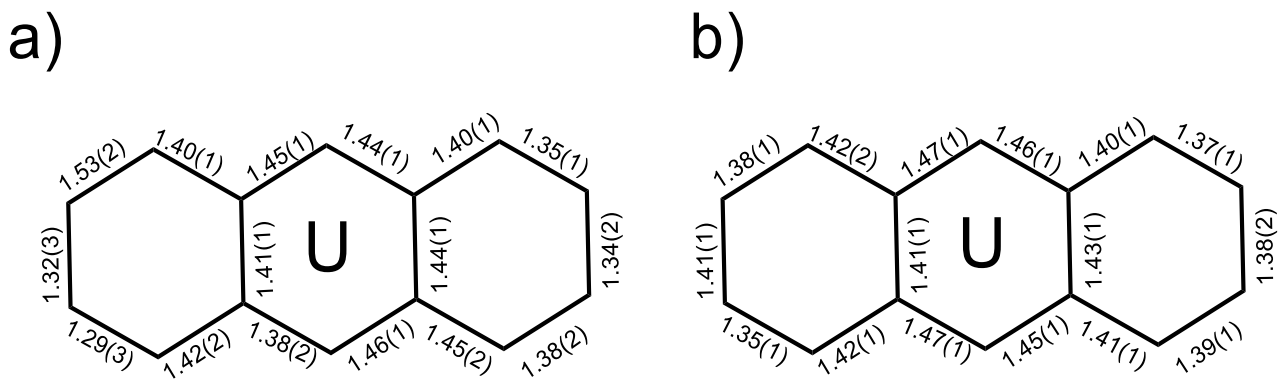

Figure S3. Carbon-carbon bond length diagrams in **3**·THF·C_6H_{14} for the a) η^6-coordinated anthracenide and b) slipped η^6-coordinated anthracenide ligands.

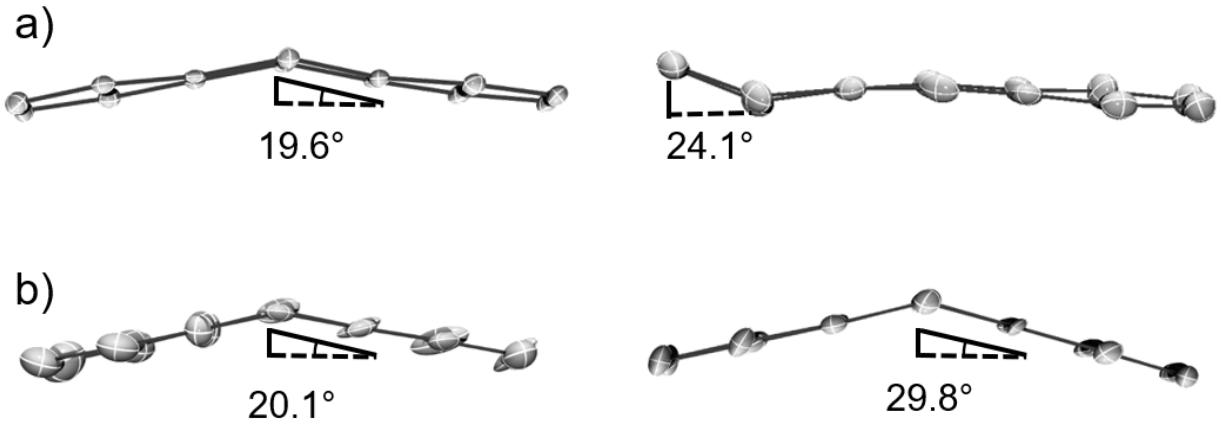

Figure S4. Ring folding angles in a) **1**·THF for the η^6-coordinated (left) and the η^4-coordinated anthracenides (right). b) **3**·THF·C_6H_{14} for the η^6-coordinated (left) and the slipped η^6-coordinated anthracenides (right).

Table S1. X-ray Crystallographic Data for **1**·THF, **2**, and **3**·THF·C_6H_{14}.

	1·THF	**2**	**3**·THF·C_6H_{14}
Empirical formula	$C_{44}H_{64}N_6O_3P_2U$	$C_{24}H_{72}I_3N_{12}O_4P_4U$	$C_{44}H_{60}O_2N_3PU$
Cryst. habit, color	block, dark purple	plate, blue	block, red
Cryst. size (mm)	0.12 × 0.11 × 0.10	0.40 × 0.3 × 0.1	0.33 × 0.24 × 0.22
Cryst. system	Triclinic	Monoclinic	Monoclinic
Space group	$P\bar{1}$	*Cc*	$P2_1/c$
volume (Å^3)	2159.3(6)	9673(1)	4076.7(5)
a (Å)	11.107(1)	22.823(2)	10.3829(7)
b (Å)	12.411(1)	26.037(2)	20.220(1)
c (Å)	17.777(3)	16.729(1)	19.423(1)
α (deg)	89.209(2)	90	90
β (deg)	73.340(2)	103.336(2)	91.291(2)
γ (deg)	67.677(2)	90	90
Z	2	4	2
Fw (g/mol)	1024.99	2668.06	931.97
Density (calcd) (Mg/m^3)	1.578	1.832	1.556
Abs coeff (mm^{-1})	3.879	5.443	4.064
F_{000}	1034.0	5132.0	1908.0
Total no. of reflns	20892	43529	88042
Unique reflns	8466	15499	9433
Final R indices [I > 2σ(I)]	R1 = 0.0325, wR2 = 0.0734	R1 = 0.0368, wR2 = 0.0935	R1 = 0.0742, wR2 = 0.1333
Largest diff peak and hole (e/Å^3)	2.37, -1.04	2.22, -2.40	2.46, -3.28
GOF	1.030	1.042	1.150

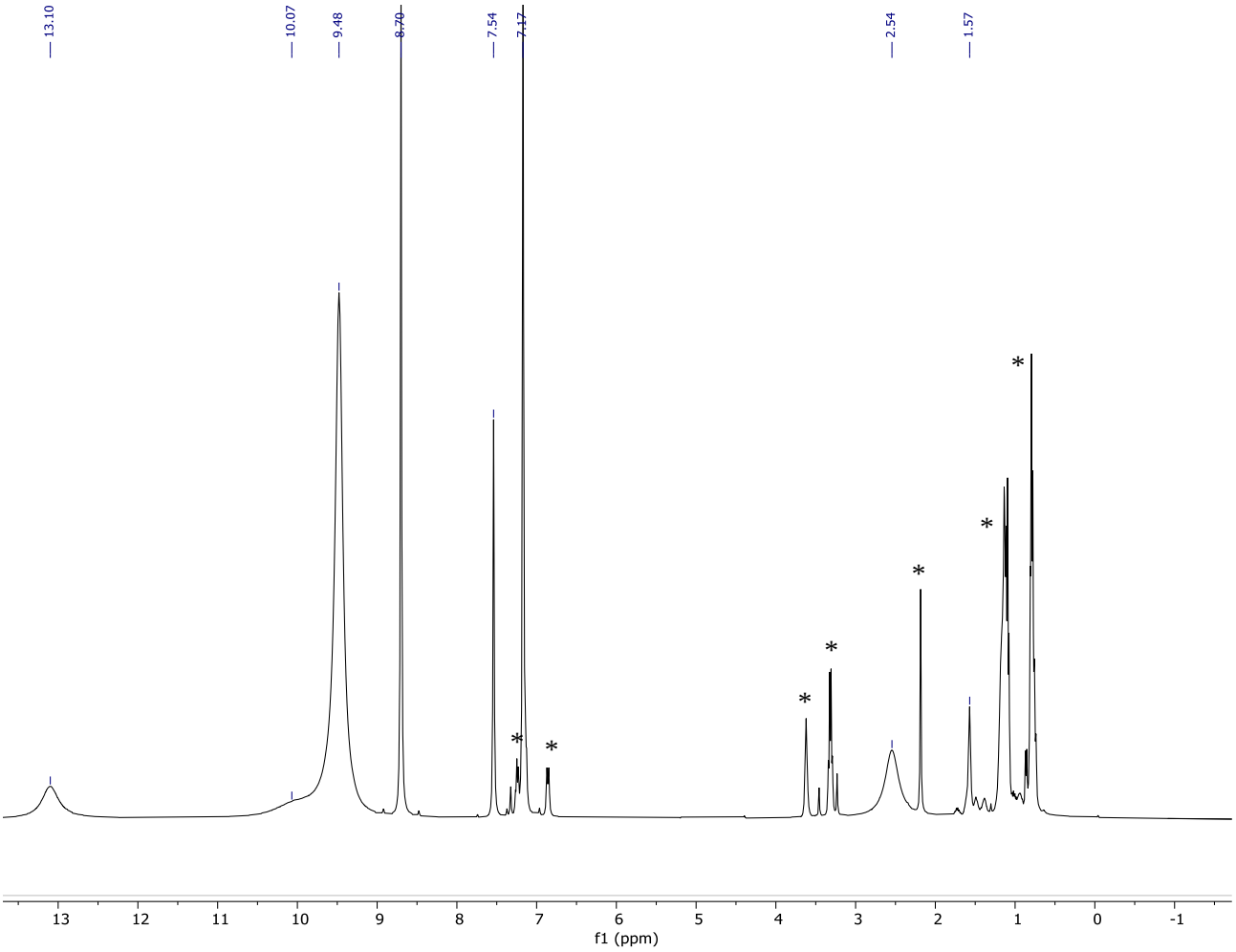

Figure S5. ^{1}H NMR spectrum of **2** in py-d_5 at 25 °C. Asterisks denote contributing resonances from residual solvents toluene, THF, Et_2O, and hexanes.

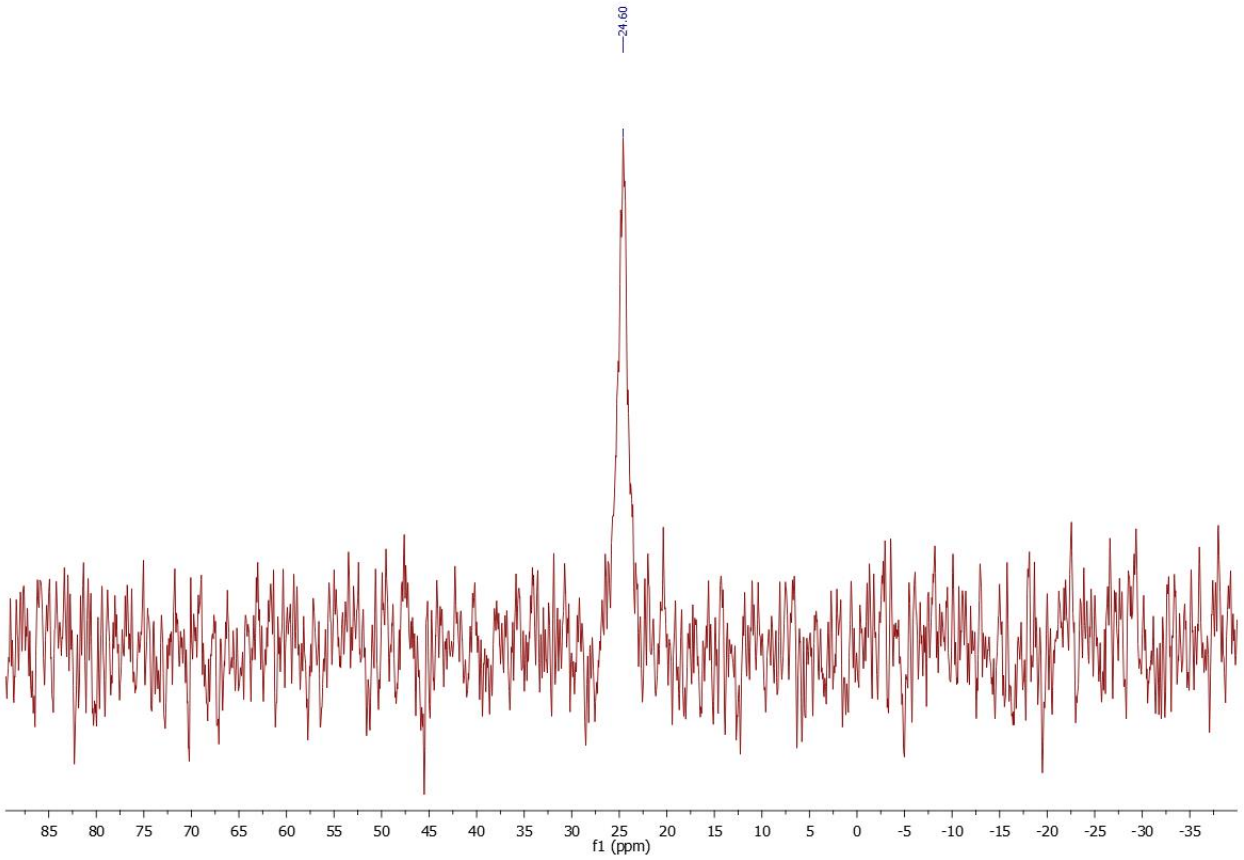

Figure S6. $^{31}P\{^{1}H\}$ NMR spectrum of **2** in py-d_5 at 25 °C.

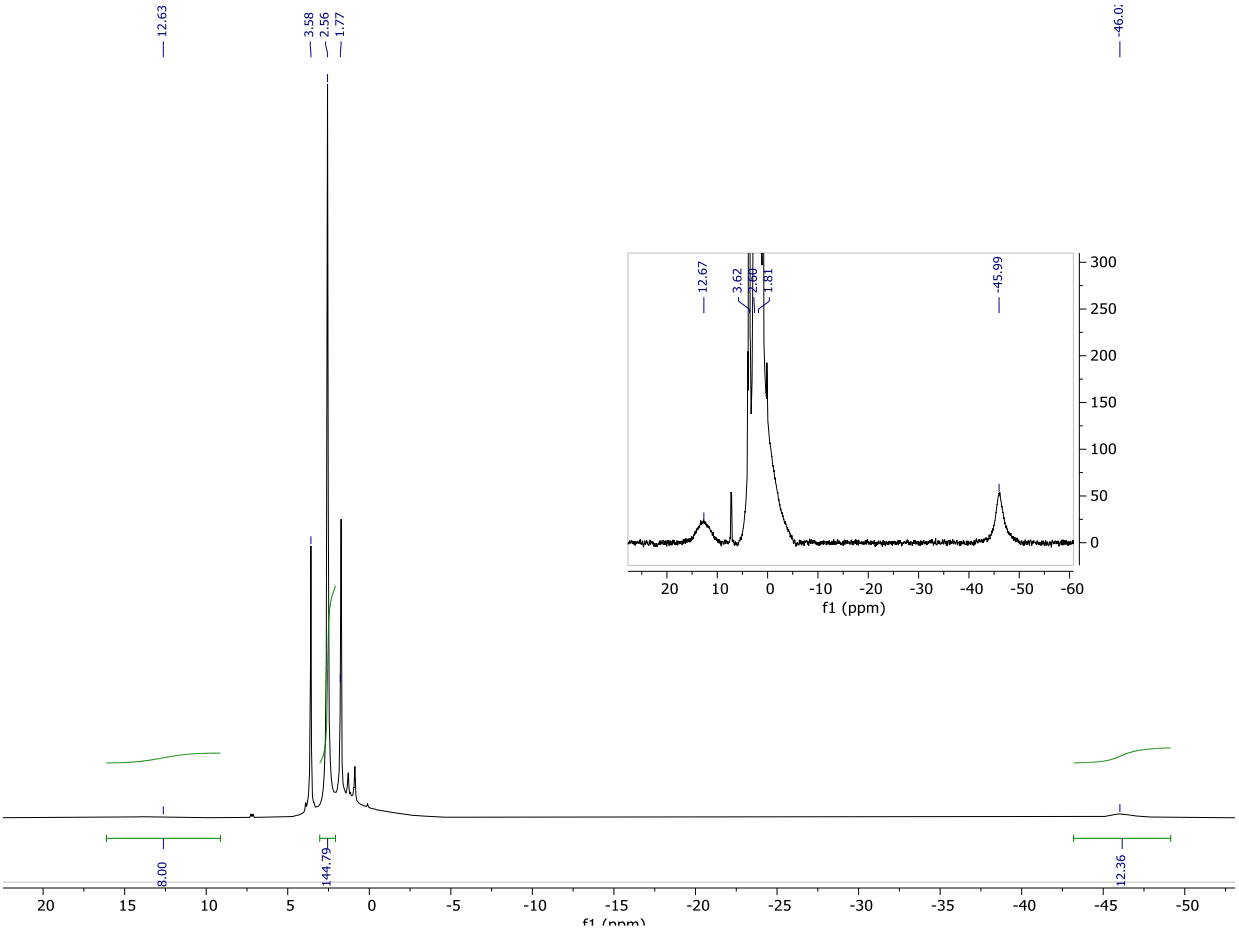

Figure S7. ^{1}H NMR spectrum of **1**·THF in THF-d_8 at 25 °C. Insert displays selected range at greater magnification.

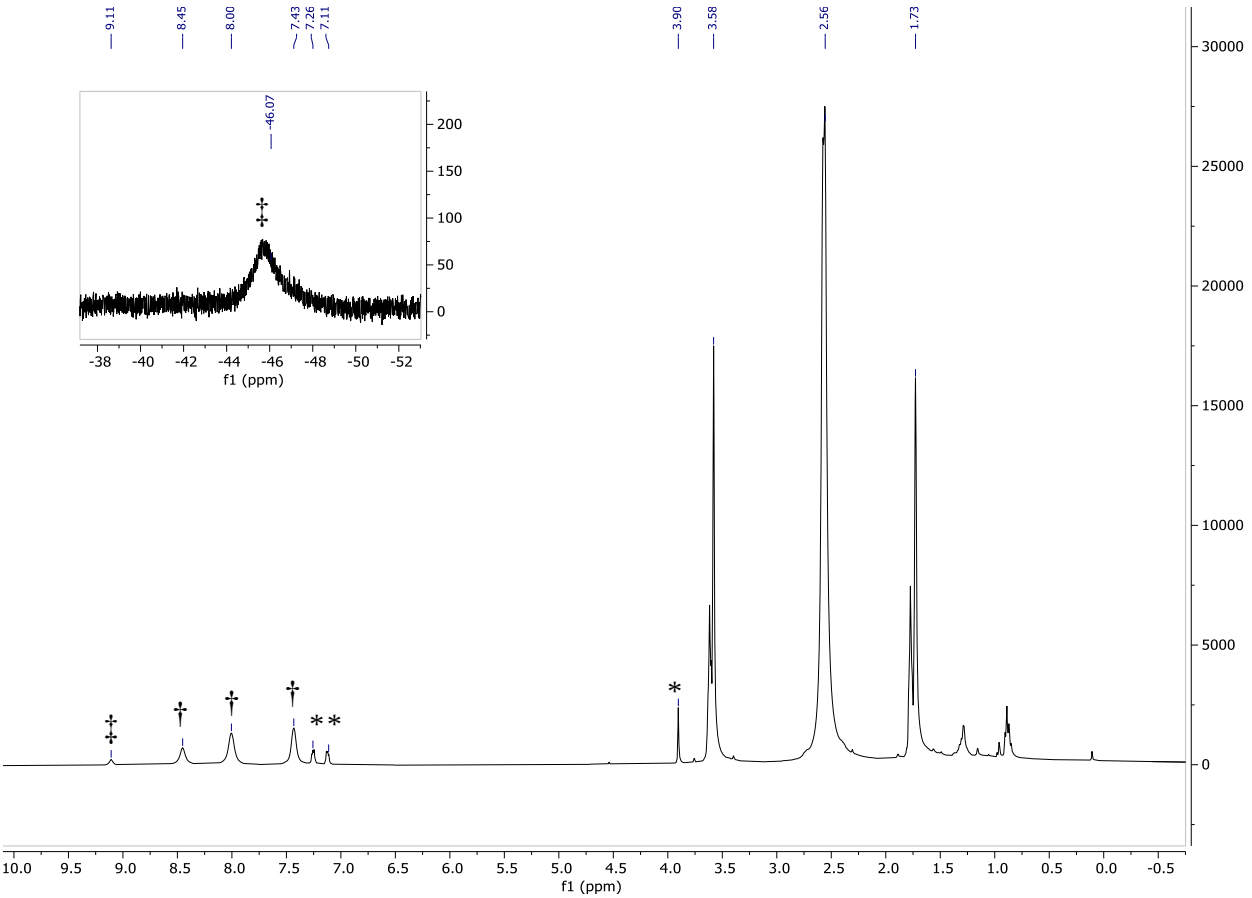

Figure S8. ^{1}H NMR spectrum of **1**·THF in THF-d_8 at 25 °C after 7 days. Resonances marked with asterisks and † denote the formation of 9,10-dihydroanthracene and anthracene, respectively, from the decomposition of **1**·THF. Resonances marked with ‡ denote the formation of a minor, unidentified, paramagnetic species.

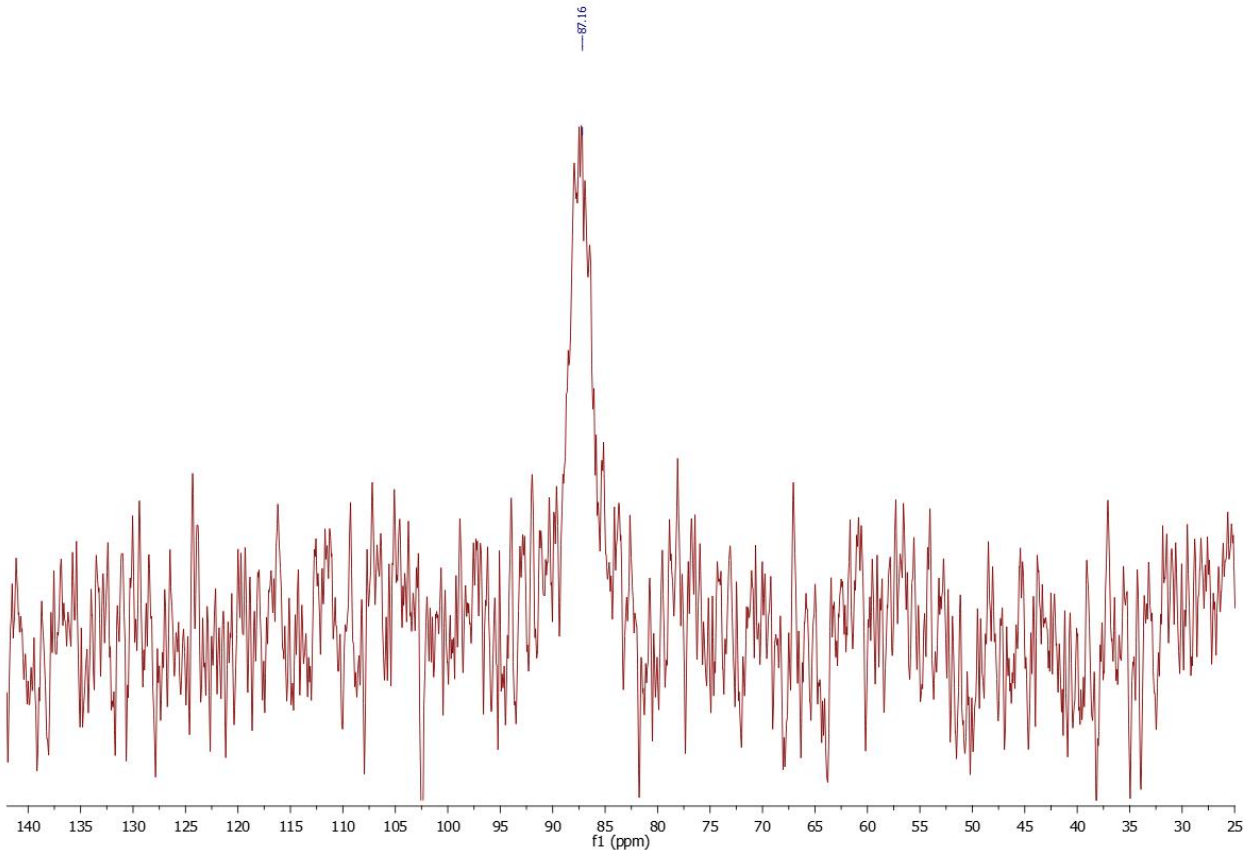

Figure S9. $^{31}P\{^{1}H\}$ NMR spectrum of **1**·THF in THF-d_8 at 25 °C.

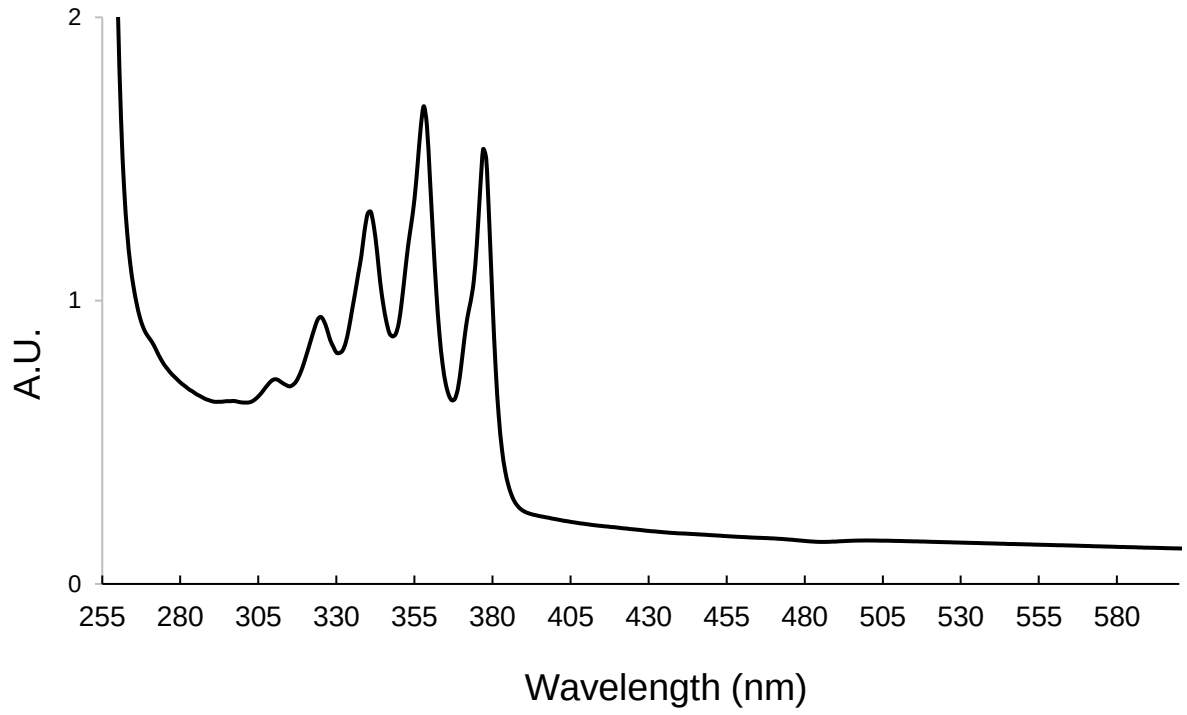

Figure S10. UV-vis spectrum of **1**·THF in THF at 25 °C.

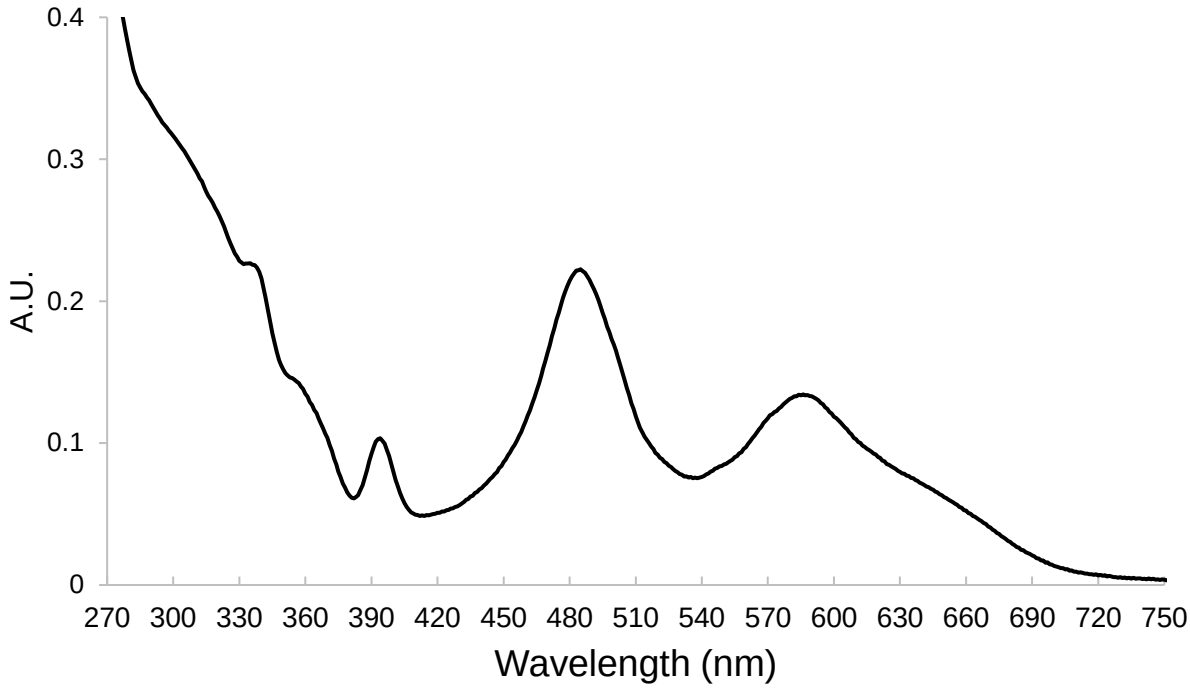

Figure S11. UV-vis spectrum of **2** in pyridine at 25 °C.

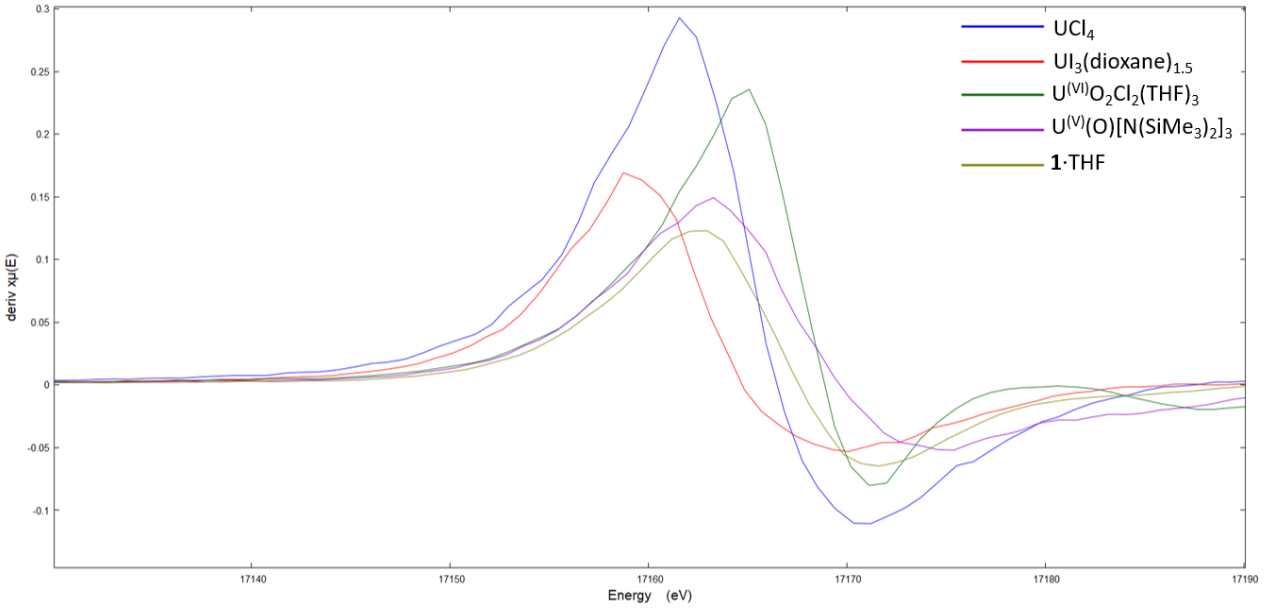

Figure S12. XANES plot of the absorption edge energies expressed as the first derivative for **1**·THF and the uranium compounds used as oxidation state reference standards.

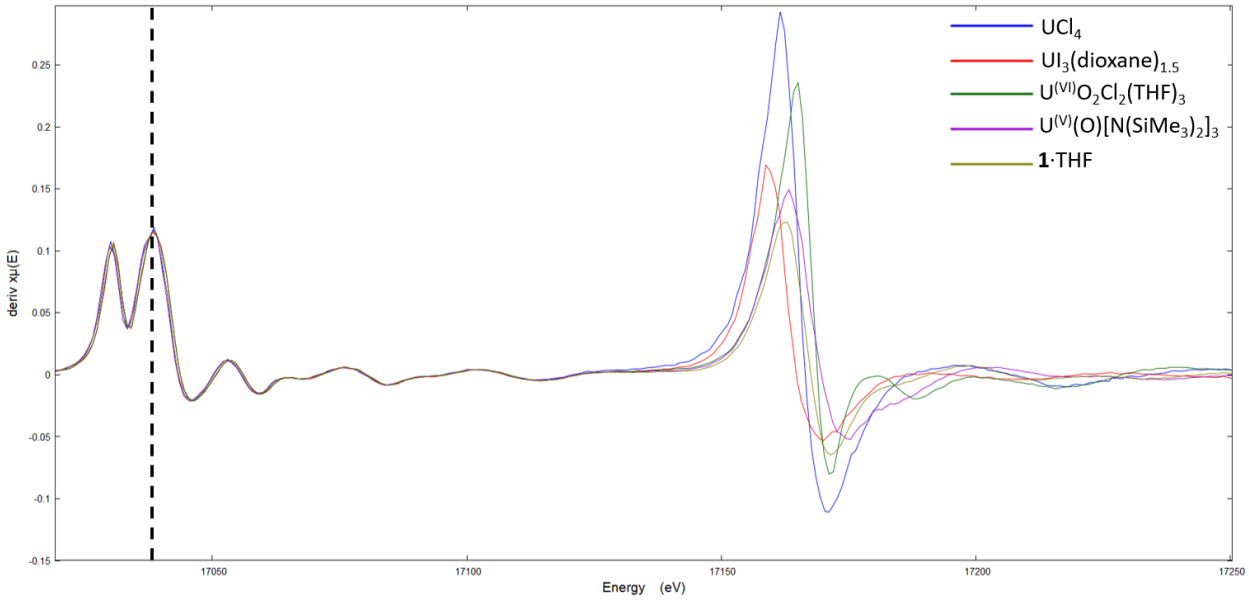

Figure S13. XANES plot of the absorption edge energies expressed as the first derivative for **1**·THF and the uranium compounds used as oxidation state reference standards with the yttrium foil reference energy alignment shown by the dotted line.

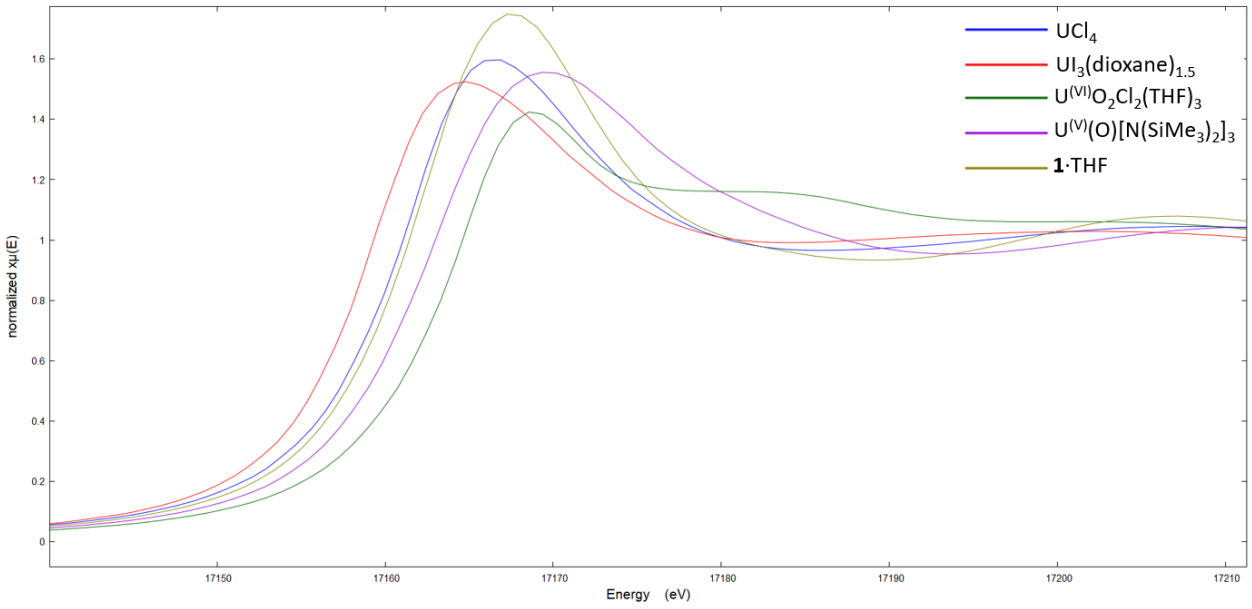

Figure S14. Normalized XANES plot of the absorption edge energies for **1**·THF and the uranium compounds used as oxidation state reference standards.

Table S2. XANES energies for **1**·THF and the uranium standards given as the edge energy at the inflection point (1st derivative) and white line values. (Yttrium foil reference at 17038.4 eV).

Compounds	Inflection Point Energy (eV)	White Line Energy (eV)
$UI_3(dioxane)_{1.5}$	17158.8	17164.8
UCl_4	17161.6	17166.4
1·THF	17162.4	17167.4
$U(O)[N(SiMe_3)_2]_3$	17163.3	17169.4
$UO_2Cl_2(THF)_3$	17165.1	17168.6

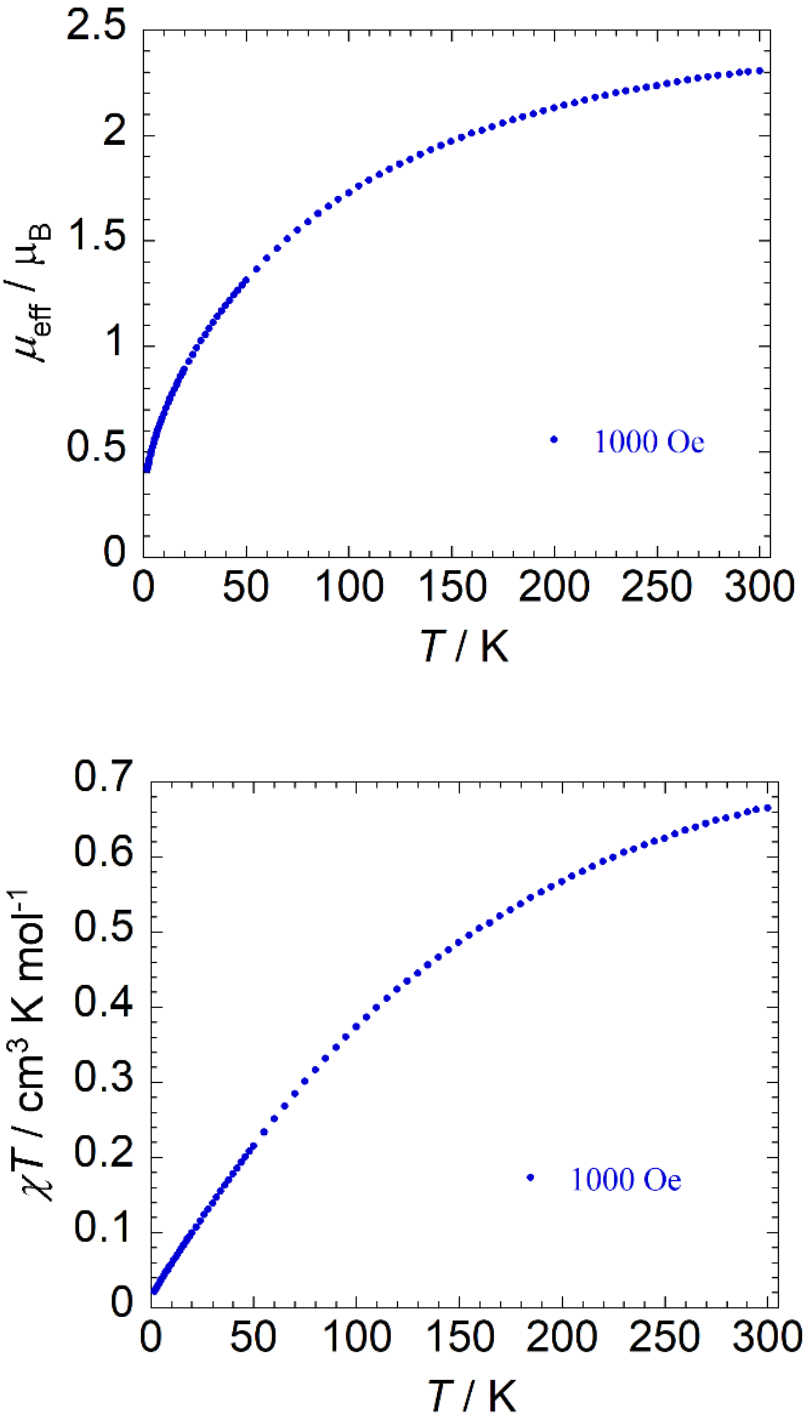

Figure S15. Effective magnetic moment (top) and temperature dependence of the χT product (bottom) at 1000 Oe for **1**·THF.

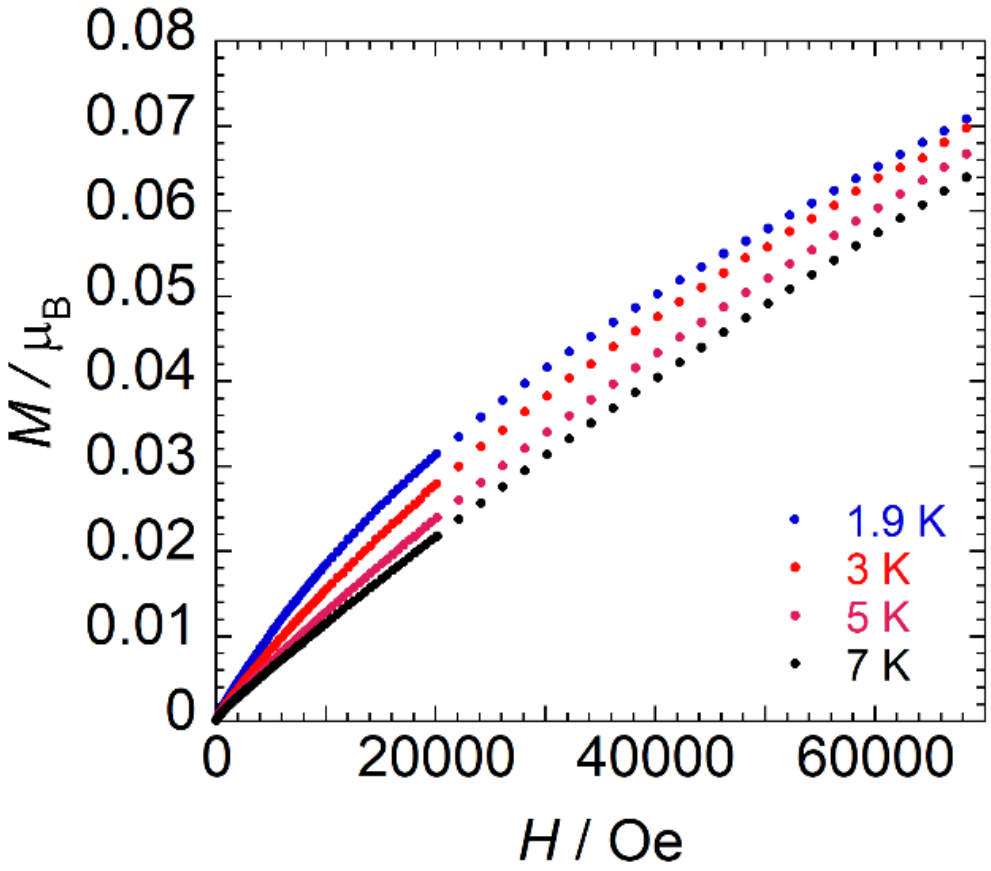

Figure S16. Solid-state field dependence of the magnetization for **1**·THF at 1.9, 3, 5, and 7 K.

Computational Details

Density functional theory (DFT) calculations were performed on [U(η^6-$C_{14}H_{10}$)(η^4-$C_{14}H_{10}$)(HMPA)$_2$],(**1**), and [U(η^6-$C_{14}H_{10}$)$_2$(HMPA)(THF)] (**3**). Geometry optimizations were performed and all structures were confirmed as minima by means of harmonic vibrational analysis as implemented in the Turbomole program package V7.3.[12] All spin states were optimized converging the Cartesian gradient to 10^{-4} a.u., with the exception of the triplet state of **1** where an additional 30 geometry steps were performed setting the threshold for the Cartesian gradient to 10^{-5} a.u. in order to obtain a structure without any negative frequencies. The PBE functional[13] and the def2-TZVP basis set were used for all atoms with the exception of uranium, where the def-TZVP basis set and its corresponding ECP were employed.[14] Grimme's D3 dispersion correction was also used.[15] The resolution of identity (RI) approximation was also employed for integral evaluation.[16] Single point energy corrections were performed in THF solvent with the same functional and basis set. Free energies were computed using standard state conditions and gas phase vibrational frequencies. These results were further analyzed by computing CM5 charges,[17] analyzing the atomic contributions to the molecular orbitals calculated using the Hirshfeld method,[18] and performing topological analysis of the electron density with Bader's Atoms in Molecules (QTAIM) as implemented in Multiwfn 3.8.[19] To calculate Mayer and Nalewajski-Mrozek bond orders, DFT single-point calculations were performed on the optimized ground state structures using the PBE functional as implemented in the Amsterdam Density Functional (ADF) program package.[20] The TZP all electron basis set was used and core orbitals were not frozen. Scalar relativistic effects were included using the zero-order regular approximation (ZORA).

The DFT (PBE) triplet and quintet geometries are both in good agreement with the experimental structures, the latter being 8.5 and 10.4 kcal/mol higher in relative energy for **1** and **3**, respectively (Table S3). The computations show **3** to be 6.9 kcal/mol higher in energy than **1** (Fig. S18). Additionally, hypothetical complexes U(η^6-$C_{14}H_{10}$)$_2$(HMPA)$_2$ (**1′**) and U(η^4-$C_{14}H_{10}$)(η^6-$C_{14}H_{10}$)(HMPA)(THF) (**3′**) were optimized by rotating one anthracenide group showing that the experimentally characterized **1** and **3** were more stable by 1.5 and 3.4 kcal/mol, respectively (Fig. S18). In addition to the differences in the orientation of the $C_{14}H_{10}$ ligands, exchanging one HMPA ligand with THF was unfavourable by 10.3 kcal/mol in **1** to form **3′** and by 5.4 kcal/mol in **1′** to form **3**. Overall, the conversion of **1** to **3** is not spontaneous, indicating that the addition of AgOTf to **1** plays

a pivotal role in the observed ring migration and ligand exchange.

In addition to the DFT calculations, the electronic structure was studied by the complete active space self-consistent field (CASSCF) method along with second-order energy corrections (CASPT2) for **1** and **3**. CASPT2 calculations were performed using the OpenMolcas 18.094 program package[21] on the geometries obtained from DFT. An ANO-RCC basis set of triple-ζ quality was used for uranium and first coordination sphere of uranium (*i.e.*, the η^6/η^4 carbons and the oxygen atoms).[22] A minimal basis set was used for peripheral carbon, nitrogen, phosphorous and hydrogen atoms. The specific contractions used were 9s8p6d4f2g1h for U, 4s3p2d1f for O, 4s3p2d1f for coordinating C atoms, 2s1p for peripheral C atoms, 2s1p for N, 3s2p for P and 1s for H. Scalar relativistic effects are included through the use of the second-order Douglas-Kroll-Hess (DKH) Hamiltonian.[23] The computation of the integrals was expedited through the use of Cholesky decomposition and local exchange screening.[24] In CASPT2, an IPEA shift of 0.25 and imaginary shift 0.2 a.u. were used.

The minimal active space would include two electrons in the seven 5*f* orbitals, denoted (2*e*,7*o*). However, this active space cannot assess uranium-anthracenide bonding; therefore, we perform calculations with a larger active space that includes 10 electrons in 15 orbitals, (10*e*,15*o*), where eight additional orbitals with ligand (anthracene) contribution and their corresponding electrons are included. These are "π-like" orbitals and can be thought of as four bonding and antibonding pairs. This active space was used to analyze the nature of bonding and the relative energies of the spin states. The effective bond order (EBO) can be computed for a pair of bonding and antibonding orbitals from the CASSCF natural orbital occupation numbers, ON, using the following equation

$$EBO = \frac{ON_{bonding} - ON_{antibonding}}{2}$$

The percent radical character of the bond can then be calculated using the following expression

$$\%rad = (1 - EBO) \times 100$$

This approach has been described in detail by us and others previously.[25]

To determine the impact of changing the U-C bond distance in **3** on the CASPT2 electronic structure, a series of Cartesian displacements were made displacing along each of the U-C distances. The step size was taken to be 1% of the U-C bond distance in the DFT optimized

structure. Actual displacements vary within the η^6-ligand since the six U-C bonds are not the same. After displacing along the U-C distance for one of the two anthracenide ligands, a constrained DFT geometry optimization was performed keeping the U-C distances in both ligands fixed. CASPT2 single point calculations were then performed on each of the structures for the triplet group state. The process was repeated for the second anthracenide ligand, keeping the U-C bond distances in the first fixed.

DFT Energies

Table S3. DFT relative energies (kcal/mol) for the RI-PBE-D3/def-TZVP,def2-TZVP optimized structures.

Spin	1	3	$\langle S^2 \rangle$ Calculated	$\langle S^2 \rangle$ Exact
Singlet	21.8[a]	22.6[a]	0	0
Triplet	0.0	0.0	2.2	2
Quintet	8.5	10.4	6.0	6
Septet	26.5	29.5	12.0	12

[a]Single point calculation on ground state triplet geometry

DFT Geometries

Table S4. Average U-C and U-O bond distances in Å for the PBE-D3 optimized geometries from the triplet, quintet, and septet spin states of **1** and **3**.

Complexes	Bonds	Exp. Geometry	Triplet Geometry	Quintet Geometry	Septet Geometry
1	U-η^6C	2.725	2.759	2.752	2.784
	U-η^4C	2.667	2.655	2.724	2.745
	U-O_{HMPA}	2.330	2.382	2.412	2.432
3	U-η^6C	2.727	2.722	2.802	2.775
	U-η^6C	2.765	2.749	2.736	2.827
	U-O_{HMPA} / U-O_{THF}	2.337/2.533	2.364/2.542	2.378/2.563	2.398/2.571

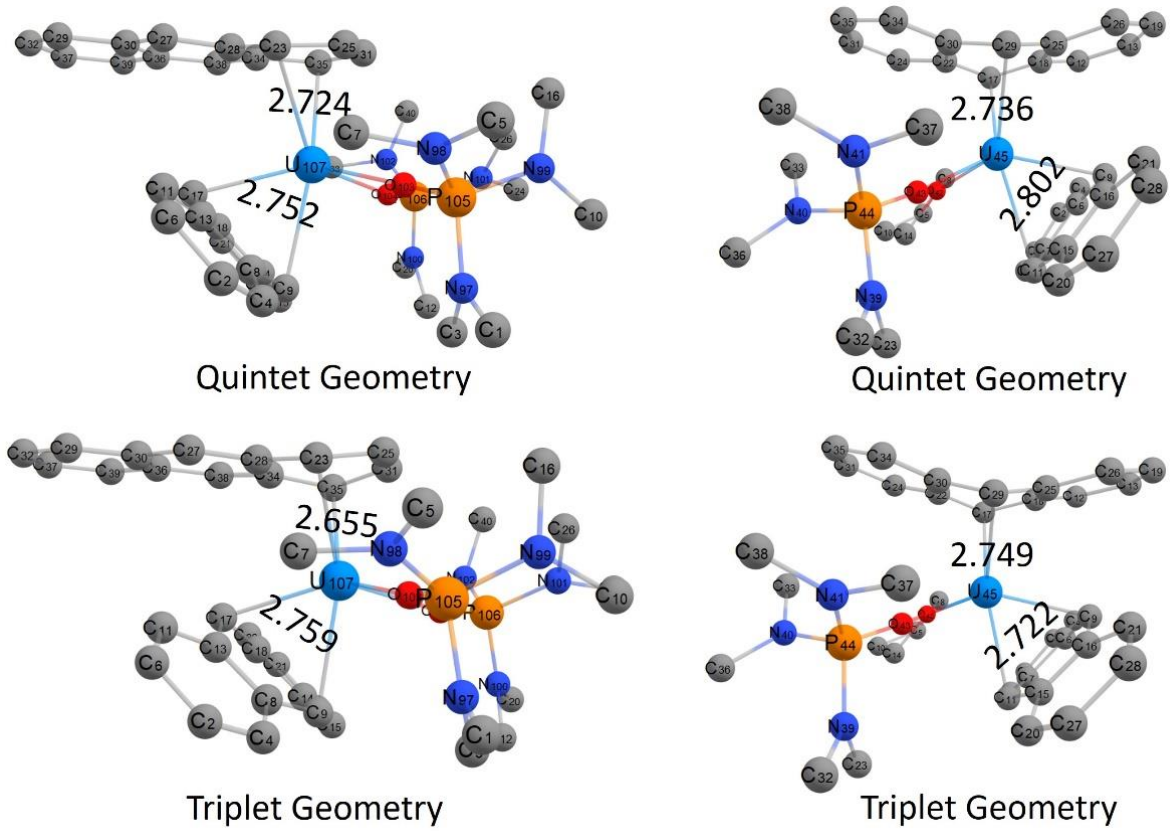

Figure S17. DFT optimized triplet and quintet geometries with the average U-C distances. Left side for complex **1** and right-side complex for **3.**

Table S5. Selected U-C and C-C bond distances and angles for PBE-D3 optimized geometries from the triplet, quintet, and septet spin states of **1**. Atom numbers labeled as shown in **Figure S17**.

Bond	Expt.	Triplet	Quintet	Septet
107U-23C	2.671	2.584	2.797	2.803
107U-25C	2.666	2.672	2.712	2.692
107U-31C	2.662	2.702	2.680	2.691
107U-35C	2.667	2.661	2.707	2.796
107U-η^4-C avg.	**2.667**	**2.655**	**2.724**	**2.745**
107U-8C	2.788	2.802	2.812	2.818
107U-9C	2.595	2.660	2.676	2.782
107U-13C	2.788	2.748	2.751	2.758
107U-14C	2.859	2.897	2.862	2.849
107U-17C	2.546	2.597	2.603	2.713
107U-18C	2.816	2.852	2.806	2.783
107U-η^6-C avg.	**2.725**	**2.759**	**2.752**	**2.784**
23C-25C*	1.431	1.436	1.412	1.411
25C-31C*	1.379	1.392	1.410	1.421
31C-35C*	1.429	1.436	1.419	1.412
35C-34C	1.461	1.452	1.438	1.434
34C-28C	1.453	1.459	1.459	1.459
28C-23C	1.466	1.450	1.434	1.436
C-C η^4 avg.	**1.436**	**1.438**	**1.429**	**1.429**
8C-9C	1.454	1.447	1.438	1.424
9C-14C	1.453	1.447	1.441	1.423
14C-18C	1.433	1.441	1.444	1.457
18C-17C	1.441	1.442	1.438	1.422
17C-13C	1.445	1.445	1.438	1.422
13C-8C	1.430	1.440	1.447	1.459
C-C η^6 avg.	**1.443**	**1.444**	**1.441**	**1.435**
$C_{centroid(\eta6)}$-U-$C_{centroid(\eta4)}$	132.8°	130.2°		
Bend in η^4 ring(31C-X-28C)	24.1°	15.5°		
Bend in η^6 ring(13C-X-14C)	19.6°	19.3°		

X is a dummy atom in the center of the ring.

Table S6. Selected U-C and C-C bond distances and angles for PBE-D3 optimized geometry from the triplet, quintet, and septet spin states of **3**. Atom numbers labeled as shown in **Figure S17.**

Bond	Expt.	Triplet	Quintet	Septet
45U-6C	2.787	2.752	2.775	2.756
45U-7C	2.851	2.818	2.893	2.856
45U-9C	2.521	2.567	2.672	2.692
45U-11C	2.625	2.639	2.835	2.805
45U-15C	2.823	2.795	2.858	2.800
45U-16C	2.754	2.760	2.781	2.743
45U-η^6_1C avg.	**2.727**	**2.722**	**2.802**	**2.775**
45U-17C	2.539	2.548	2.578	2.746
45U-18C	2.830	2.793	2.822	2.824
45U-22C	2.919	2.875	2.784	2.883
45U-25C	2.823	2.809	2.837	2.842
45U-29C	2.544	2.571	2.592	2.766
45U-30C	2.935	2.899	2.802	2.901
45U-η^6_2C avg.	**2.765**	**2.749**	**2.736**	**2.827**
6C-7C	1.440	1.443	1.451	1.458
7C-11C	1.446	1.439	1.424	1.421
11C-15C	1.375	1.443	1.426	1.422
15C-16C	1.400	1.443	1.451	1.458
16C-9C	1.439	1.439	1.428	1.425
9C-6C	1.437	1.441	1.430	1.422
C-C η^6_1 avg.	**1.423**	**1.441**	**1.435**	**1.434**
29C-25C	1.459	1.457	1.450	1.428
25C-18C	1.415	1.438	1.440	1.454
18C-17C	1.465	1.456	1.448	1.428
17C-22C	1.448	1.456	1.448	1.427
22C-30C	1.438	1.441	1.448	1.459
30C-29C	1.459	1.455	1.448	1.426
C-C η^6_2 avg.	**1.447**	**1.450**	**1.447**	**1.437**
$C_{centroid(\eta6)}$-U-$C_{centroid(\eta6)}$	134.1°	135°		
Bend in η^6_1 ring(6C-X-15C)	20.1°	13.3°		
Bend in η^6_2 ring(18C-X-30C)	29.8°	25.1°		

X is a dummy atom in the center of the ring.

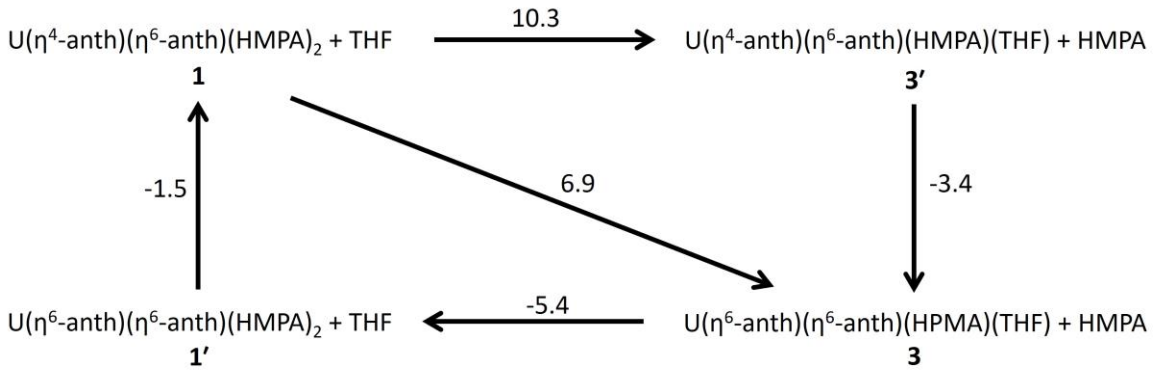

Figure S18. The Gibb's free energy (in kcal/mol) of reaction between **1**, **1′**, **3**, and **3′** at the RI-PBE/def2-TZVP, def-TZVP level of theory (gas phase geometry optimizations and single point with THF as the solvent. Standard state corrections for THF as the solvent are included)

CASPT2 Energies

Table S7: CASPT2 relative energies (kcal/mol) using the (10*e*,15*o*) active space. Energies were computed on two different structures of **1** and **3** optimized at the DFT level of theory.

	1		**3**	
Spin States	**Triplet Geometry**	**Quintet Geometry**	**Triplet Geometry**	**Quintet Geometry**
Singlet	16.2	30.3	14.1	21.5
Triplet	3.2	0.0	2.9	0.0
Quintet	10.8	9.4	15.6	16.1
Septet	55.2	41.2	51.6	47.7

CASSCF Active Orbitals

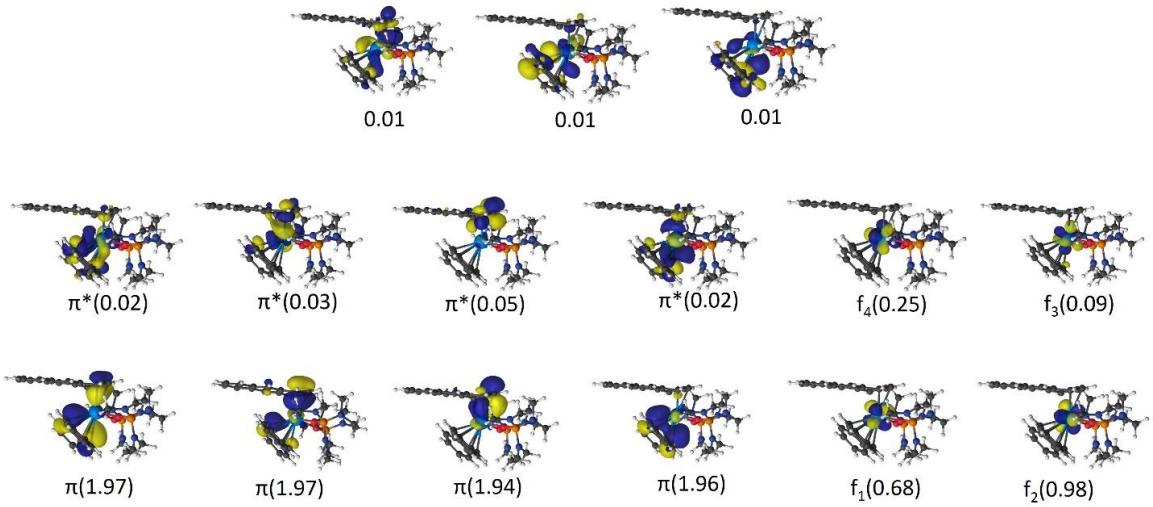

Figure S19. The CASSCF (10*e*,15*o*) natural orbitals are shown for the singlet state computed on the triplet geometry for **1**. Occupation numbers are in parentheses. An isovalue of 0.04 was used.

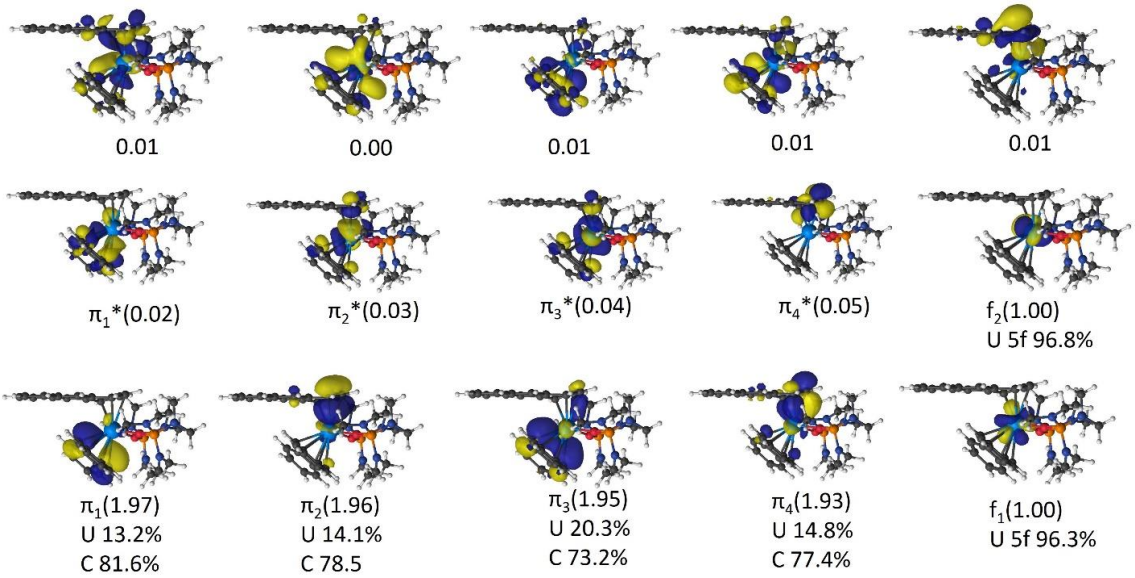

Figure S20. The CASSCF (10*e*,15*o*) natural orbitals are shown for the triplet state computed on the triplet geometry for **1**. Occupation numbers are in parentheses and the Hirshfeld contribution of U and coordinated C atoms are shown for the bonding orbitals. An isovalue of 0.04 was used.

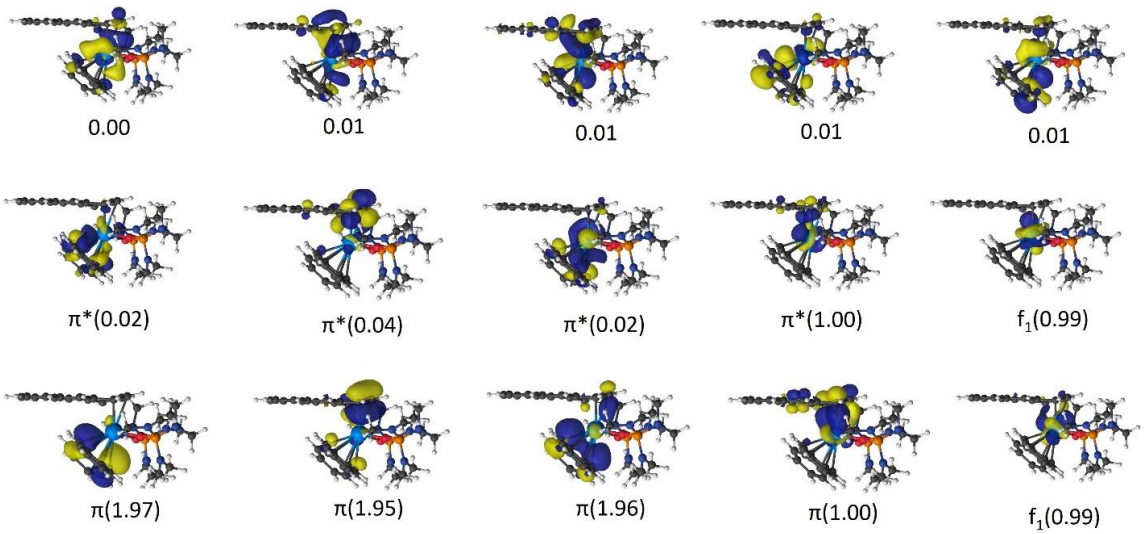

Figure S21. The CASSCF (10*e*,15*o*) natural orbitals are shown for the quintet state computed on the triplet geometry for **1**. Occupation numbers are in parentheses. An isovalue of 0.04 was used.

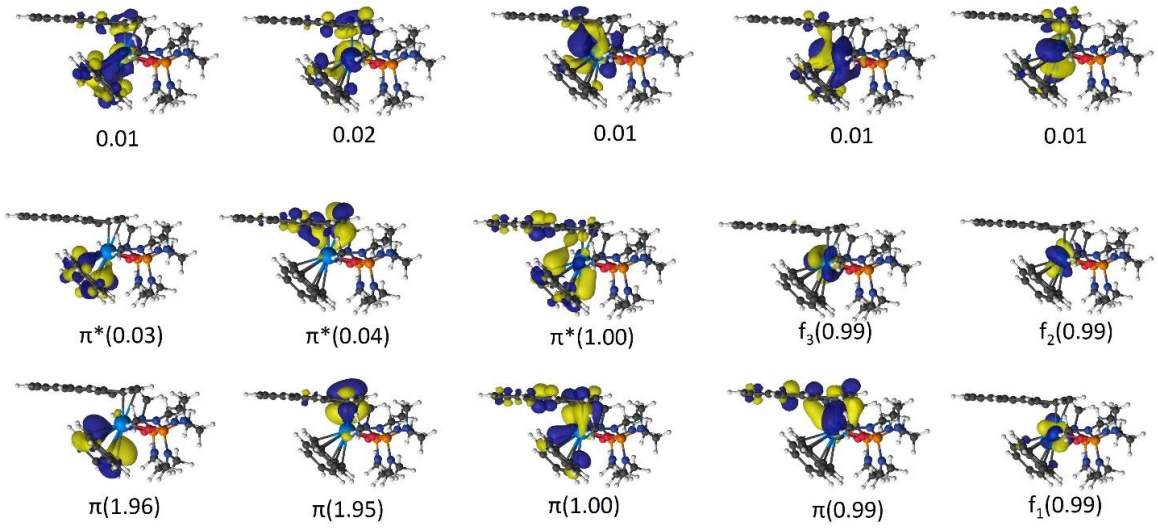

Figure S22. The CASSCF (10*e*,15*o*) natural orbitals are shown for the septet state computed on the triplet geometry for **1**. Occupation numbers are in parentheses. An isovalue of 0.04 was used.

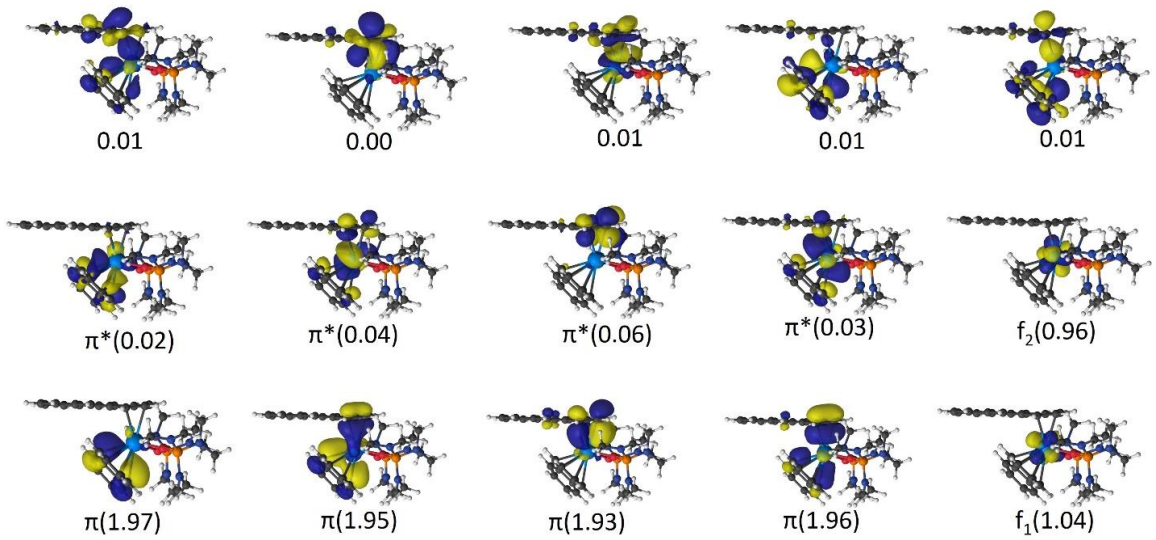

Figure S23. The CASSCF (10*e*,15*o*) natural orbitals are shown for the singlet state computed on the quintet geometry for **1**. Occupation numbers are in parentheses. An isovalue of 0.04 was used.

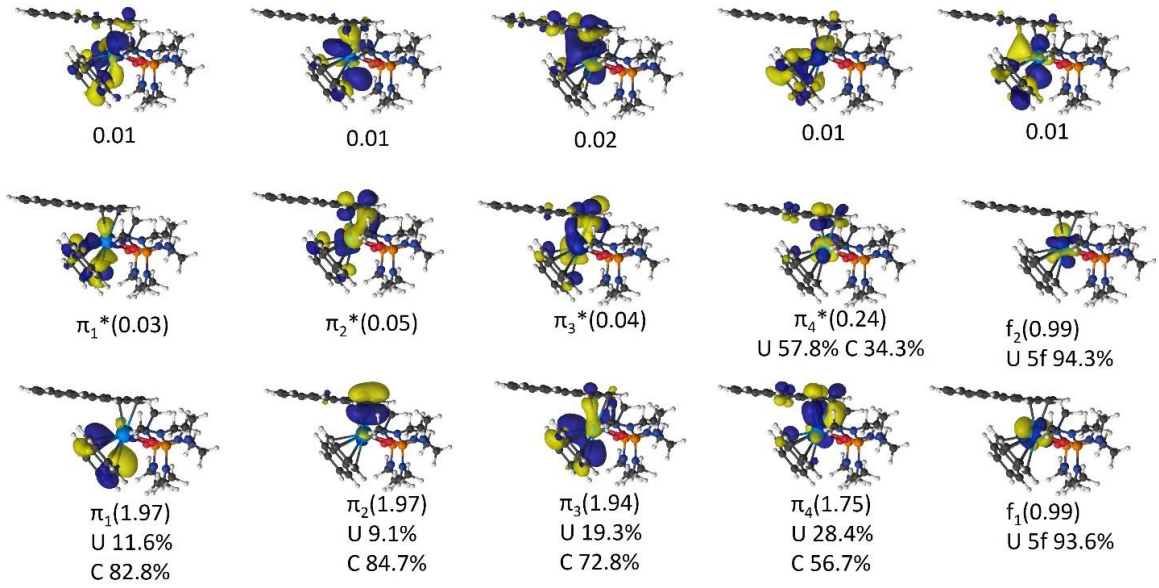

Figure S24. The CASSCF (10*e*,15*o*) natural orbitals are shown for the triplet state computed on the quintet geometry for **1**. Occupation numbers are in parentheses and the Hirshfeld contribution of U and coordinated C atoms are shown for the bonding orbitals. An isovalue of 0.04 was used.

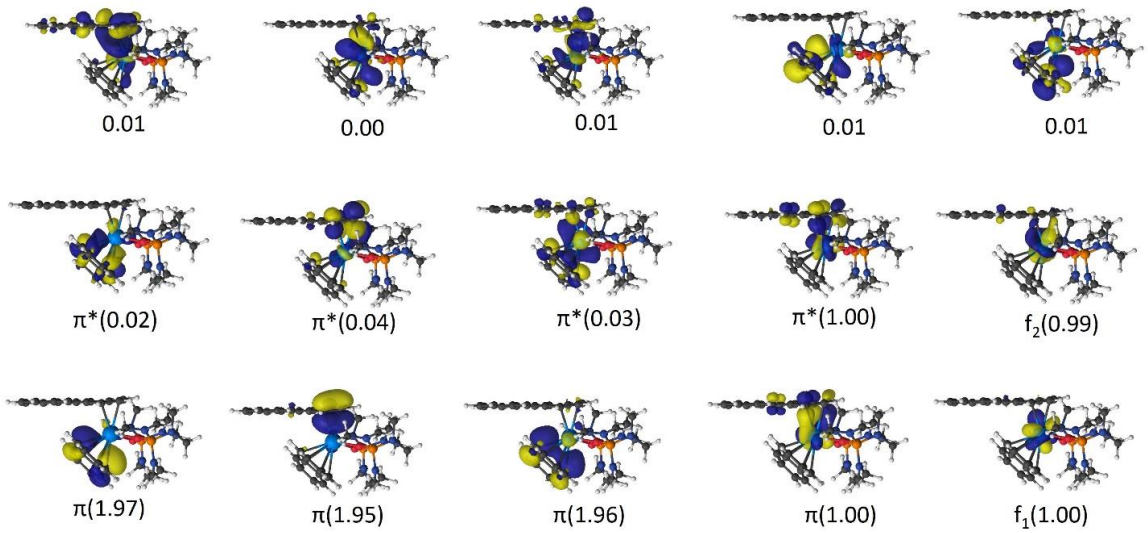

Figure S25. The CASSCF (10*e*,15*o*) natural orbitals are shown for the quintet state computed on the quintet geometry for **1**. Occupation numbers are in parentheses. An isovalue of 0.04 was used.

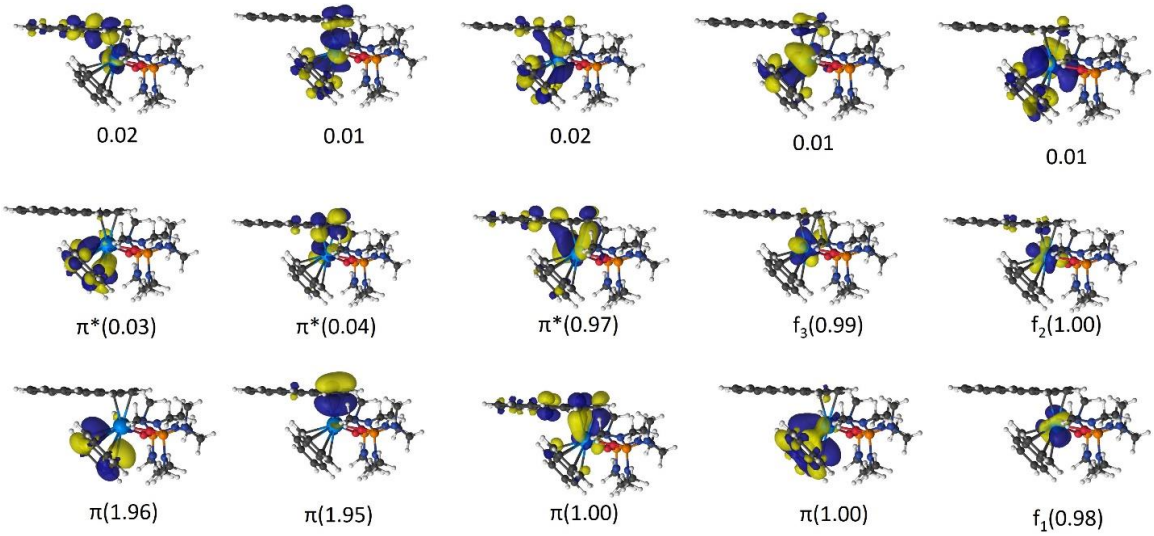

Figure S26. The CASSCF (10*e*,15*o*) natural orbitals are shown for the septet state computed on the quintet geometry for **1**. Occupation numbers are in parentheses. An isovalue of 0.04 was used.

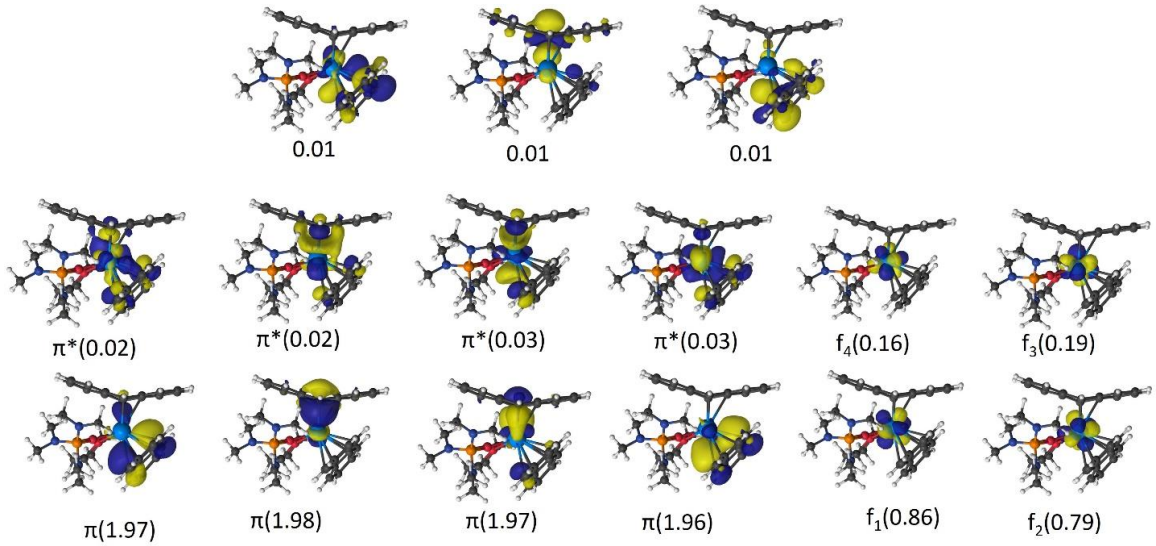

Figure S27. The CASSCF (10*e*,15*o*) natural orbitals are shown for the singlet state computed on the triplet geometry for **3**. Occupation numbers are in parentheses. An isovalue of 0.04 was used.

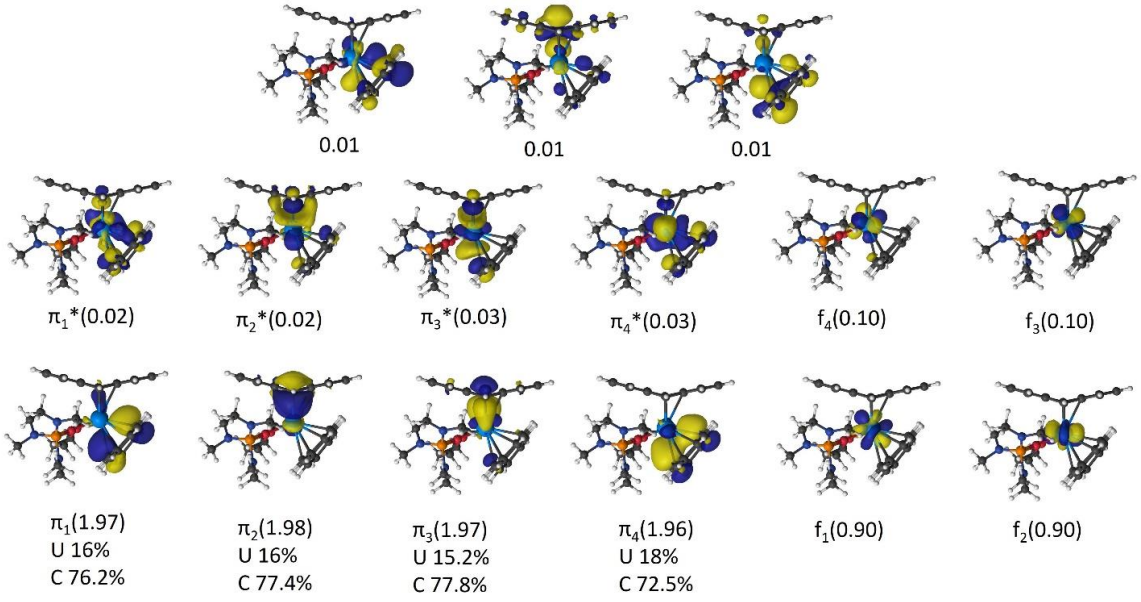

Figure S28. The CASSCF (10*e*,15*o*) natural orbitals are shown for the triplet state computed on the triplet geometry for **3**. Occupation numbers are in parentheses and the Hirshfeld contribution of U and coordinated C atoms are shown for the bonding orbitals. An isovalue of 0.04 was used.

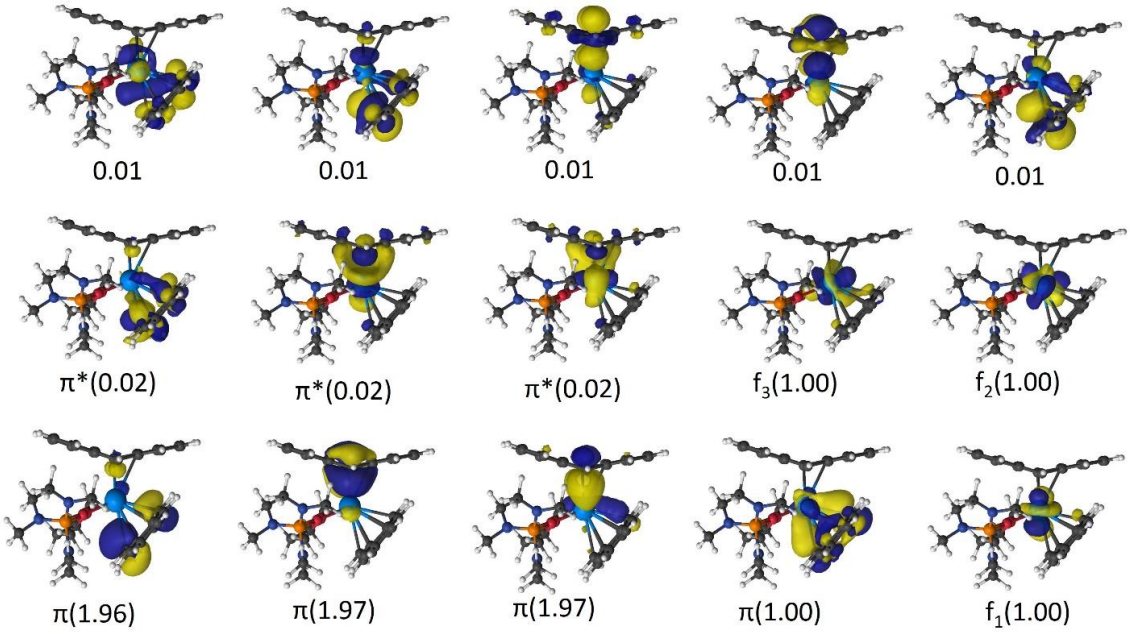

Figure S29. The CASSCF (10*e*,15*o*) natural orbitals are shown for the quintet state computed on the triplet geometry for **3**. Occupation numbers are in parentheses. An isovalue of 0.04 was used.

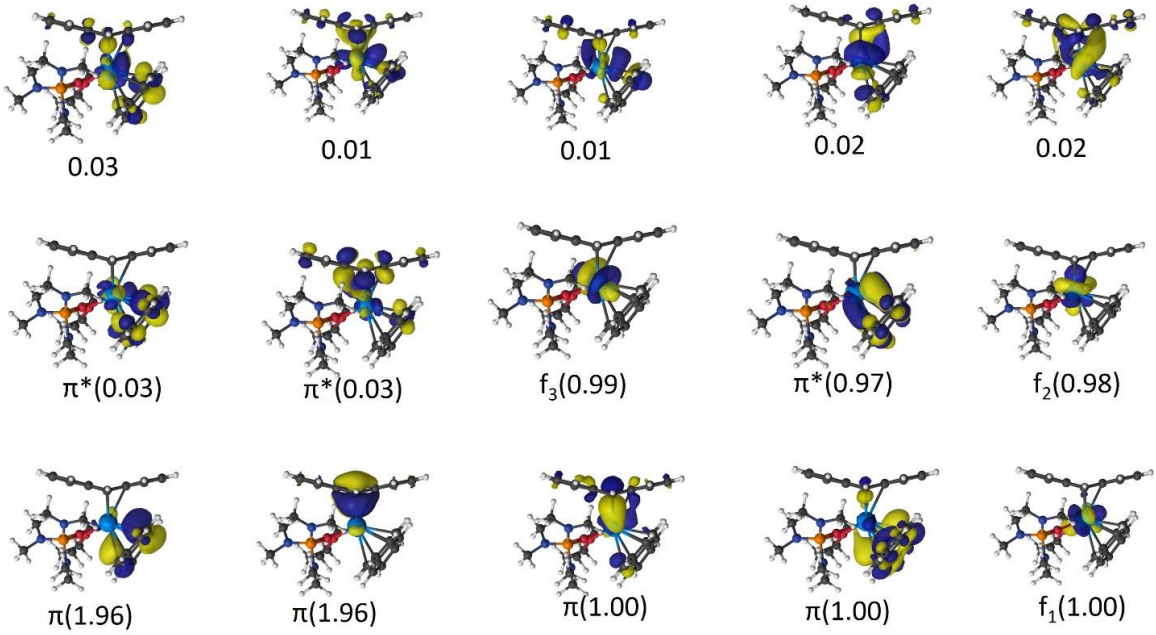

Figure S30. The CASSCF (10*e*,15*o*) natural orbitals are shown for the septet state computed on the triplet geometry for **3**. Occupation numbers are in parentheses. An isovalue of 0.04 was used.

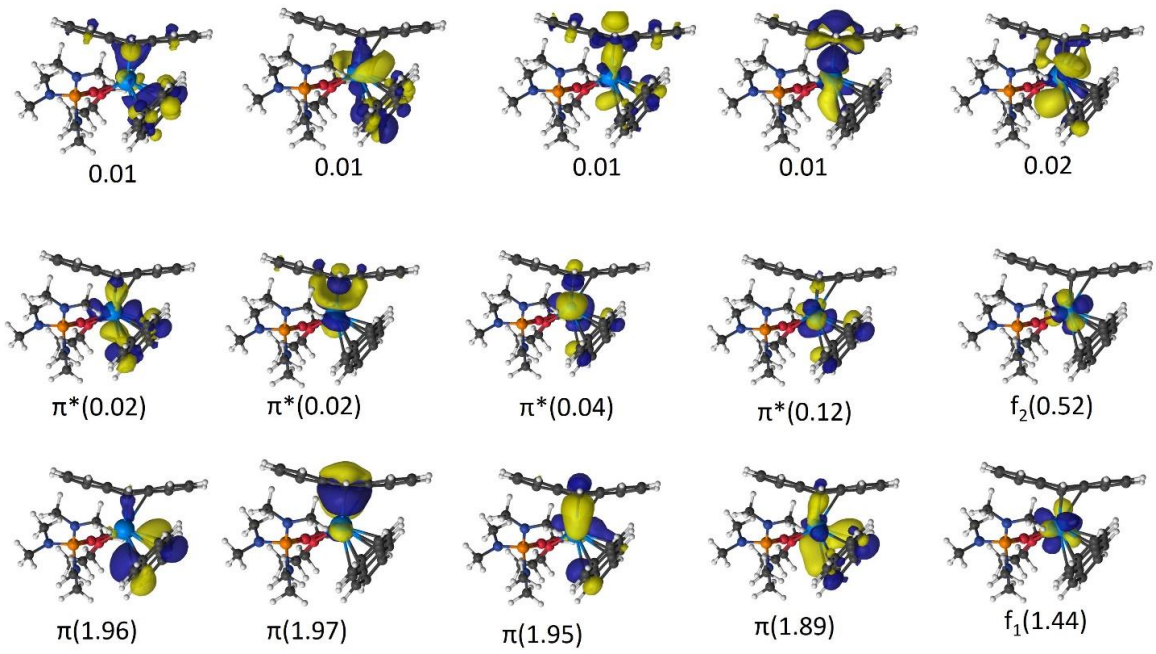

Figure S31. The CASSCF (10*e*,15*o*) natural orbitals are shown for the singlet state computed on the quintet geometry for **3**. Occupation numbers are in parentheses. An isovalue of 0.04 was used.

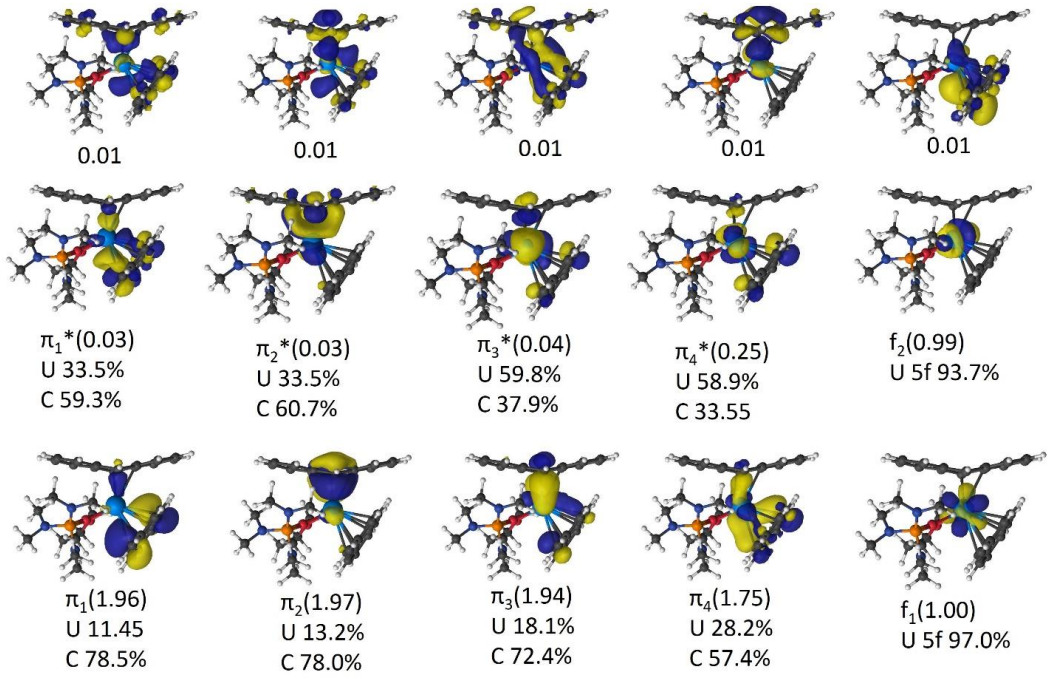

Figure S32. The CASSCF (10*e*,15*o*) natural orbitals are shown for the triplet state computed on the quintet geometry for **3**. Occupation numbers are in parentheses and the Hirshfeld contribution of U and coordinated C atoms are included for bonding orbitals. An isovalue of 0.04 was used.

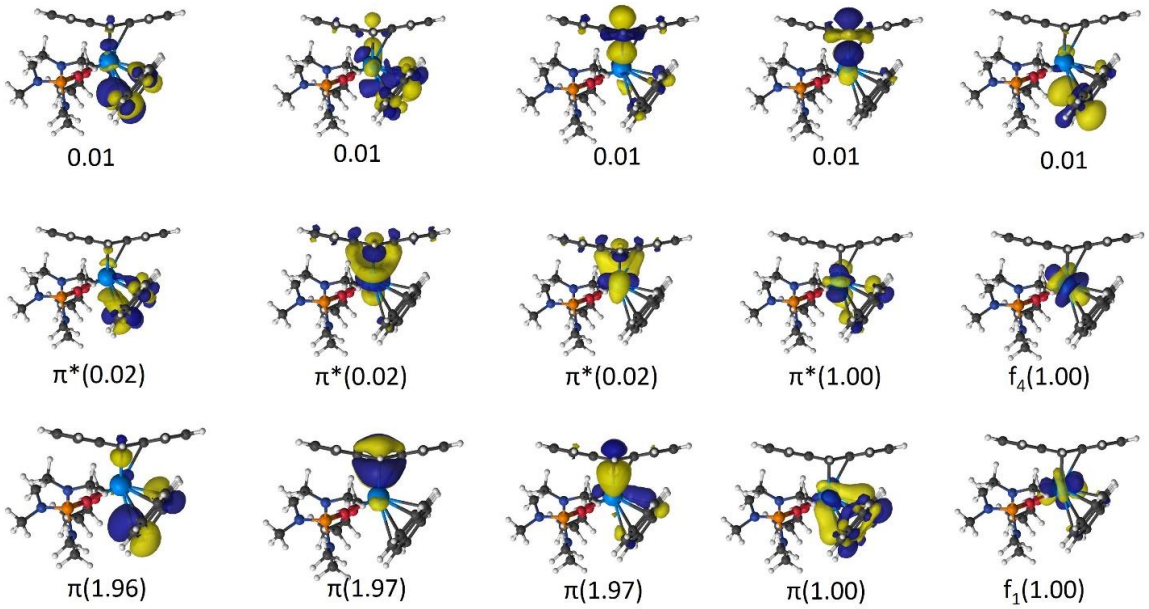

Figure S33. The CASSCF (10*e*,15*o*) natural orbitals are shown for the quintet state computed on the quintet geometry for **3**. Occupation numbers are in parentheses. An isovalue of 0.04 was used.

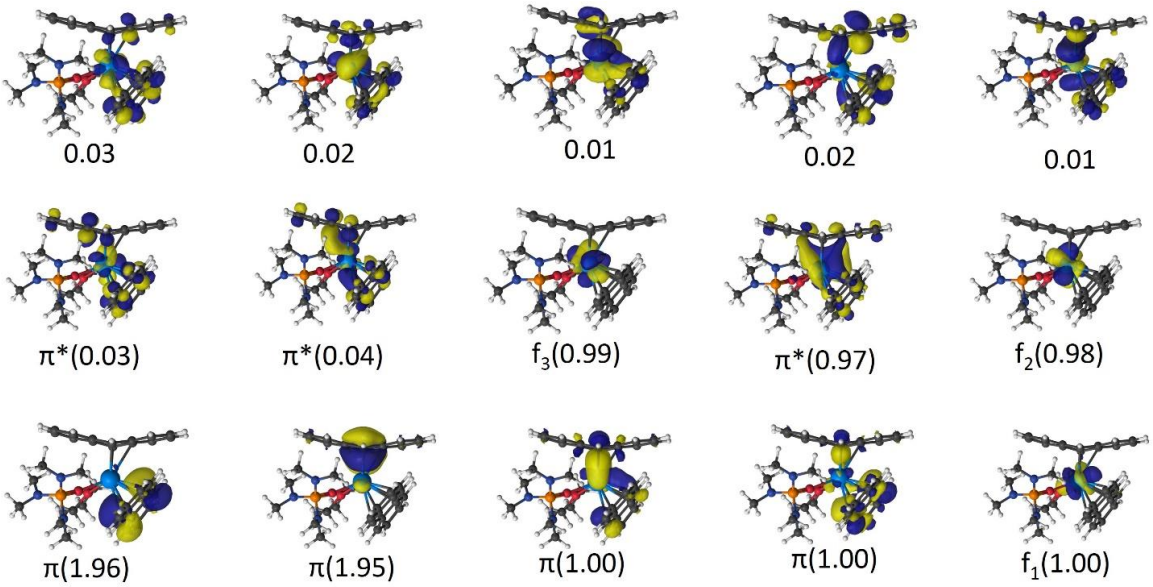

Figure S34. The CASSCF (10*e*,15*o*) natural orbitals are shown for the septet state computed on the quintet geometry for **3**.. Occupation numbers are in parentheses. An isovalue of 0.04 was used.

CASSCF Spin Density

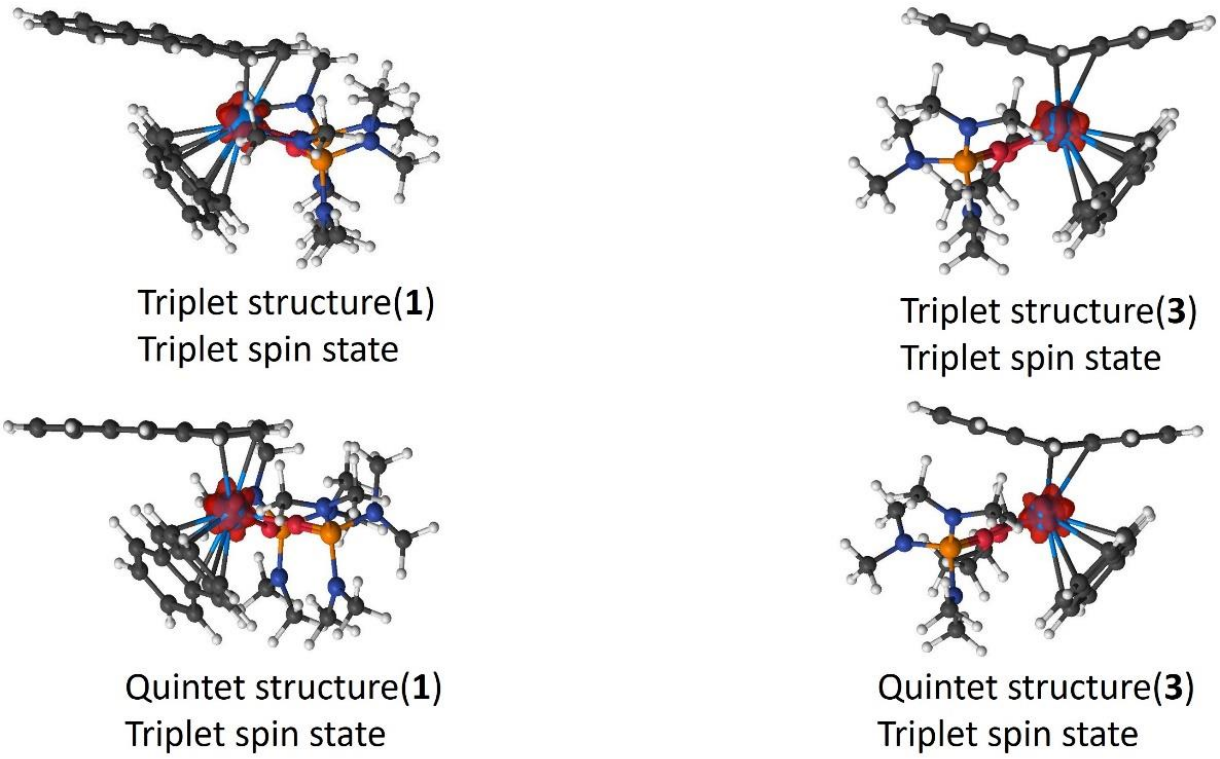

Figure S35. CASSCF spin density for complex **1** and **3** for the triplet state computed on both the triplet geometry (top) and quintet geometry (bottom).

CASSCF Wavefunctions

Table S8. Dominant CI configurations contributing to the total CASSCF wavefunction for **1**.

Spin State	Configuration	Triplet Geometry	Quintet Geometry
Singlet	$\pi^8 f_1^2$	31.2%	43.5%
	$\pi^8 f_2^2$	45.3%	47%
	$\pi^8 f_3^2$	11.5%	
Triplet	$\pi^8 f_1^1 f_2^1$	90.2%	77%
	$\pi^6 f_1^1 f_2^1 \pi_4^{*2}$	1.4%	5.4%
	$\pi^6 \pi_4^1 f_1^1 f_2^1 \pi_4^{*1}$		3.6%
Quintet	$\pi^6 \pi^1 f_1^1 f_2^1 f_3^1$	92.9%	92.5%
Septet	$\pi^4 \pi^1 \pi^1 f^1 f^1 f^1 \pi^{*1}$	92.2%	91.2%

Table S9. Dominant CI configurations contributing to the total CASSCF wavefunction for **3.**

Spin State	Configuration	Triplet Geometry	Quintet Geometry
Singlet	$\pi^8 f_1^2$	40.4%	
	$\pi^8 f_2^2$	36.9%	23.1%
	$\pi^8 f_3^2$	8.8%	63.8%
	$\pi^8 f_4^2$	7.6%	
Triplet	$\pi^8 f_1^1 f_2^1$		77.4%
	$\pi^6 f^1 f^1 \pi_4{*}^2$	84%	5.6%
	$\pi^6 \pi_4^1 f^1 f^1 \pi_4{*}^1$		4.2%
Quintet	$\pi^6 \pi^1 f^1 f^1 f^1$	93.8%	93.9%
Septet	$\pi^4 \pi^1 \pi^1 f^1 f^1 f^1 \pi{*}^1$	90.7%	90.4%

Table S10. CASPT2 single point calculations for the triplet state on each displacement from the DFT quintet geometry (taken as the zero energy in the table). Here the U-L_1 is displaced and the U-L_2 bond distance is constant at the geometry from the reference. The average U-C distance is in experiment 2.727Å and 2.65Å for U-L_1 and U-L_2 bond, respectively.

Cartesian Displacement	ΔE CASPT2 kcal/mol	$\pi_{U\text{-}C}$ Occupation	$\pi^*_{U\text{-}C}$ Occupation	Avg. U-C distance(Å)
-0.06	0.1	1.87	0.11	2.634
-0.05	-0.7	1.86	0.12	2.662
-0.04	-2.0	1.85	0.14	2.690
-0.03	-1.9	1.83	0.16	2.718
-0.02	-1.0	1.83	0.15	2.746
-0.01	-1.2	1.8	0.19	2.774
0.0	0.0	1.75	0.25	2.802
+0.01	0.6	1.76	0.24	2.830
+0.02	1.8	1.72	0.27	2.858

Table S11. CASPT2 single point calculations for the triplet state on each displacement from the DFT quintet geometry (taken as the zero energy in the table). Here the U-L_2 is displaced and the U-L_1 bond distance is constant at the geometry from the reference. The average U-C distance is in experiment 2.727 Å and 2.650 Å for U-L_1 and U-L_2 bond, respectively.

Cartesian Displacement	**ΔE CASPT2 kcal/mol**	**$\pi_{U\text{-}C}$ Occupation**	**$\pi^*_{U\text{-}C}$ Occupation**	**Avg. U-C distance(Å)**
-0.04	-1.1	1.82	0.16	2.626
-0.03	-1.3	1.82	0.17	2.654
-0.02	-1.4	1.80	0.18	2.681
-0.01	-1.0	1.79	0.20	2.708
0.0	0.0	1.75	0.25	2.736
+0.01	0.5	1.77	0.22	2.763
+0.02	1.6	1.77	0.23	2.790

DFT Charges and Orbital Analysis

Table S12. CM5 atomic charges calculated with PBE-D3 for ground state. Atom numbers labeled in Figure S1.

1				**3**			
η^6-anth	**charge**	**η^4-anth**	**charge**	**$\eta 1^6$-anth**	**charge**	**$\eta 6_2$-anth**	**charge**
1C	-0.180475	25C	-0.180475	1C	-0.118461	12C	-0.095518
2C	-0.171062	31C	-0.171062	2C	-0.12279	13C	-0.110854
3C	-0.222482	23C	-0.222482	3C	-0.113557	19C	-0.109931
4C	-0.207099	35C	-0.207099	4C	-0.098148	26C	-0.095869

6C	-0.033944	28C	-0.033944	6C	-0.054357	17C	-0.237859
7C	-0.02871	34C	-0.02871	7C	-0.048538	18C	-0.044621
9C	-0.108734	27C	-0.108734	9C	-0.210385	22C	-0.040046
11C	-0.114295	38C	-0.114295	11C	-0.215243	25C	-0.041215
15C	-0.01785	30C	-0.01785	15C	-0.051689	29C	-0.233293
16C	-0.016693	36C	-0.016693	16C	-0.050648	30C	-0.035759
20C	-0.111289	29C	-0.111289	20C	-0.112812	24C	-0.106854
21C	-0.111523	39C	-0.111523	21C	-0.097453	31C	-0.119331
27C	-0.120785	32C	-0.120785	27C	-0.1215	34C	-0.108052
28C	-0.118715	37C	-0.118715	28C	-0.121332	35C	-0.118702
46H	0.083202	71H	0.083202	46H	0.085311	53H	0.092792
47H	0.083387	78H	0.083387	47H	0.086392	55H	0.090001
48H	0.084535	87H	0.084535	48H	0.08357	62H	0.090052
49H	0.081005	90H	0.081005	49H	0.093396	71H	0.092742
57H	0.085762	76H	0.085762	57H	0.09094	58H	0.08805
59H	0.085659	93H	0.085659	59H	0.080908	77H	0.085584
64H	0.086347	79H	0.086347	64C	0.08231	63H	0.087597
66H	0.086306	84H	0.086306	66C	0.093431	73H	0.086347
70H	0.086924	91H	0.086924	70H	0.082202	84H	0.085707
72H	0.086759	95H	0.086759	72H	0.086327	85H	0.08451
SUM	**-0.65**	**SUM**	**-0.71**	**SUM**	**-0.67**	**SUM**	**-0.61**
U	0.97	O	-0.39	U	0.97	O	-0.40

DFT Orbitals

Figure S36 and **Figure S37** show the DFT frontier molecular orbitals for **1** and **3**. The two unpaired electrons are in uranium 5*f* orbitals that have contributions primarily from uranium, although a small contribution from carbon atoms is present (note that only the contributions from the carbon atoms that coordinate to uranium are included in the percentages reported). The HOMO-2, HOMO-3 and HOMO-4 orbitals contain more obvious mixing between the uranium and carbon atomic orbitals. For example, the HOMO-2, HOMO-3, HOMO-4, and HOMO-5 consist of contributions of 31.4%, 27.9%, 16.7% and 14.6% uranium, respectively. The remaining orbitals and other lower energy orbitals are anthracene based, which is consistent with the observed bond distortions due to ligand reductions. Similar results were observed for **3**.

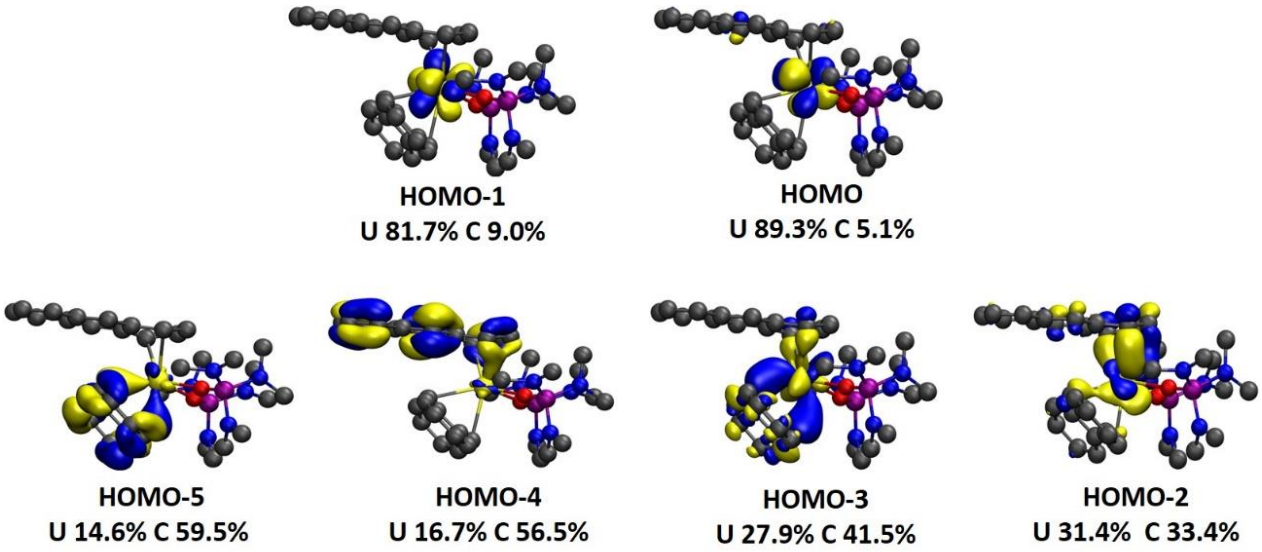

Figure S36. DFT α molecular orbitals (MOs) for **1**. The Hirshfeld atomic contributions to the molecular orbitals are also shown (only contributions from the carbon atoms coordinate to the uranium are reported). HOMO and HOMO-1 are singly occupied MOs. Hydrogen atoms are omitted for clarity.

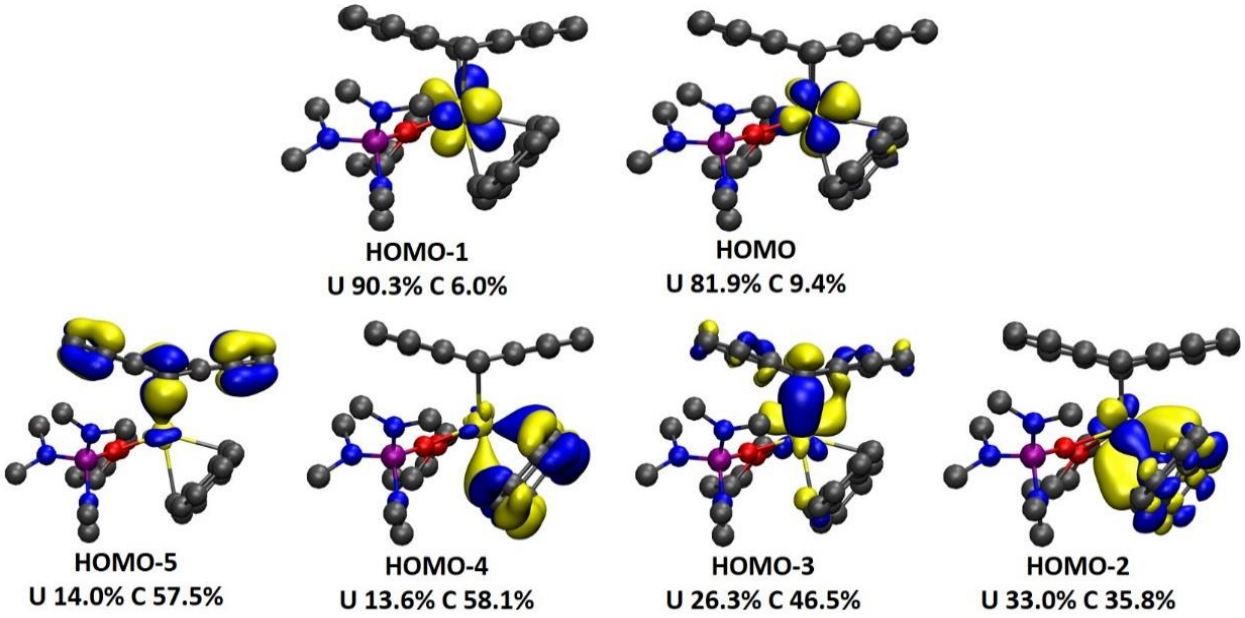

Figure S37. DFT α molecular orbitals (MOs) for **3**. The Hirshfeld atomic contributions to the molecular orbitals are also shown (only contributions from the carbon atoms coordinate to the uranium are reported). HOMO and HOMO-1 are singly occupied MOs. Hydrogen atoms are omitted for clarity.

DFT Spin Density

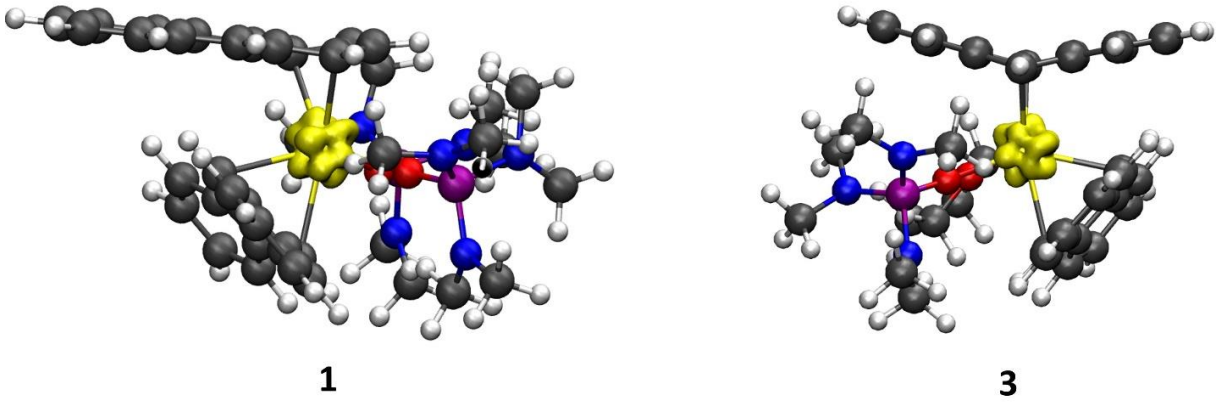

Figure S38. RI-PBE-D3/def2-TZVP, def-TZVP on U spin densities for **1** and **3** from the ground state triplet calculations

DFT QTAIM

To further understand the nature of the chemical bonding in **1** and **3**, we analyzed the topology of the electron density using the quantum theory of atoms in molecules (QTAIM) which was developed by Bader.[26] In QTAIM, a chemical bond is present if a line of locally maximum electron density joins neighboring atoms. A bond critical point (BCP) is a point along the bond path where the electron density reaches a minimum. At a BCP, the gradient (ρ) of the electron density is zero and the Laplacian of the electron density, $\nabla^2(\rho)$, could be positive or negative. A positive Laplacian means a local depletion of charge while a negative value corresponds to a local concentration of charge.

In a covalent bond, the Laplacian should be negative since it is a sign of shared interaction of electron density between two linked atoms. A closed-shell interaction is associated with a positive Laplacian and these types of bonds generally are not considered covalent due to depletion of charge at the location of the BCP. The total electronic energy density, E(r), at the BCP is defined as the sum of the Lagrangian kinetic energy, G(r), and the potential energy density, V(r). In clear cases, when E(r) and the Laplacian electron density are both negative, the bond is covalent. In less clear cases, the Laplacian is positive and the E(r) is negative then the bond is considered to be dative. On the other hand, if E(r) is close to zero, then the bond is considered to be metallic. Finally, if E(r) is positive, the bond would be identified as ionic or Van der Waals.

In **1** and **3**, for each η6 ring, we found two bond critical points. These two critical points were observed for the two shortest U-C bonds distances. For the other anthracene that is coordinated through an η4 interaction, three bond critical points were found. In every case, the energy density is negative and the Laplacian is positive, which is indicative of U-C dative bonds. In a dative bond, one of the atoms shares two electrons with another atom. This makes sense for our systems where we expected a negatively charged anthracene to share electrons with an electron deficient uranium. In **Table S13**, all the parameters from the topological analysis are given.

Table S13. Properties at the bond critical points for the **1** and **3**. All values are expressed in atomic units. Atom numbers labeled in **Figure S17**.

Compounds	Bonds	$\nabla^2(\rho)$	G(r)	V(r)	E(r)	ρ
1	U107-C25	0.11582	0.03537	-0.04179	-0.00642	0.04529
	U107-C23	0.09027	0.03585	-0.04914	-0.01329	0.05940
	U107-C35	0.09716	0.03287	-0.04145	-0.00858	0.04906
	U107-C17	0.07939	0.03495	-0.05005	-0.01510	0.06262
	U107-C9	0.07318	0.02940	-0.04050	-0.01110	0.05339

3	U45-C29	0.07790	0.03473	-0.04998	-0.01525	0.06265
	U45-C17	0.07624	0.03601	-0.05296	-0.01695	0.06601
	U45-C9	0.08368	0.03188	-0.04283	-0.01096	0.05374
	U45-C11	0.09085	0.03726	-0.05181	-0.01455	0.06211

DFT Bond Orders

Table S14. Bond order of uranium and coordinated carbon atoms in **1** and **3** (PBE). Atom numbers labeled in **Figure S17**.

Bonds	Distance	Mayer	G-J	N-M(1)	N-M(2)	N-M(3)
107U-23C	2.5834	0.5464	0.4951	0.6443	0.8253	0.6314
107U-25C	2.6725	0.3419	0.316	0.4076	0.5378	0.3958
107U-31C	2.702	0.329	0.2959	0.3814	0.503	0.3697
107U-35C	2.6612	0.4966	0.4377	0.5692	0.7537	0.5579
107U-η4C avg.		**0.428**	**0.386**	**0.501**	**0.655**	**0.489**
107U-8C	2.8629	0.1969	0.1598	0.2051	0.1989	0.1949
107U-9C	2.6479	0.5109	0.4757	0.62	0.8197	0.6094
107U-13C	2.8112	0.205	0.159	0.204	0.2013	0.194
107U-14C	2.8846	0.1942	0.154	0.1976	0.1915	0.1878
107U-17C	2.5723	0.5553	0.501	0.6522	0.8228	0.6383
107U-18C	2.8305	0.1973	0.1477	0.1895	0.1838	0.1801
U-η^4C Avg.	**2.768**	**0.310**	**0.266**	**0.345**	**0.403**	**0.334**
45U-6C	2.7516	0.2513	0.1863	0.2404	0.2377	0.2282

45U-7C	2.8176	0.2283	0.1808	0.2334	0.2243	0.2213
45U-9C	2.5665	0.5353	0.4974	0.651	0.8203	0.635
45U-11C	2.6387	0.4811	0.4644	0.6083	0.8037	0.5955
45U-15C	2.7943	0.2459	0.1904	0.2458	0.2397	0.2332
45U-16C	2.7595	0.2385	0.177	0.2284	0.222	0.2166
45U-$\eta^6{}_1$C avg.		0.330	0.283	0.368	0.425	0.355
45U-17C	2.5477	0.5682	0.5487	0.719	0.9226	0.7053
45U-18C	2.7931	0.2024	0.1771	0.2285	0.2182	0.2167
45U-22C	2.8757	0.1692	0.1448	0.1868	0.1819	0.1772
45U-25C	2.8086	0.1965	0.1776	0.2291	0.2156	0.2171
45U-29C	2.5703	0.5474	0.532	0.697	0.9017	0.6837
45U-30C	2.8984	0.1546	0.1363	0.1759	0.1668	0.1667
45U-$\eta^6{}_2$C avg.		0.306	0.286	0.373	0.434	0.361

References

[1] M. J. Monreal, R. K. Thomson, T. Cantat, N. E. Travia, B. L. Scott, J. L. Kiplinger, *Organometallics* **2011**, *30*, 2031-2038.

[2] J. L. Kiplinger, D. E. Morris, B. L. Scott, C. J. Burns, *Organometallics* **2002**, *21*, 5978-5982.

[3] S. Fortier, J. L. Brown, N. Kaltsoyannis, G. Wu, T. W. Hayton, *Inorg. Chem.* **2012**, *51*, 1625-1633.

[4] M. P. Wilkerson, C. J. Burns, R. T. Paine, B. L. Scott, *Inorg. Chem.* **1999**, *38*, 4156-4158.

[5] C.U. Segre, N.E. Leyarovska, L.D. Chapman, W.M. Lav-ender, P.W. Plag, A.S. King, A.J. Kropf, B.A. Bunker, K.M. Kemner, P. Dutta, R.S. Duran and J. Kaduk, CP521, Synchrotron Radiation Instrumentation: Eleventh U.S. National Conference, ed. P. Pianetta, et al., p419-422, (American Insitute of Physics, New York, 2000).

[6] B. Ravel, M. Newville, *J. Synchrotron Radiat.* **2005**, *12*, 537-541.

[7] SMART Apex II,Version 2.1; Bruker AXS Inc.: Madison, WI

[8] SAINT Software User's Guide,Version 7.34a; Bruker AXS Inc.: Madison, WI

[9] Blessing, R.Acta Crystallogr. A1995, A51

[10] Sheldrick, G. M. SHELXTL,6.12; Bruker Analytical X-Ray Systems, Inc.: Madison, WI

[11] Dolomanov, O. V.; Bourhis, L. J.; Gildea, R. J.; Howard, J. A. K.; Puschmann, H. *J. Appl. Cryst.*, **2009**, *42*, 339

[12] R. Ahlrichs, M. Bar, M. Haser, H. Horn, C. Kolmel, *Chem. Phys. Lett.* **1989**, *162*, 165-169.

[13] J. P. Perdew, K. Burke, M. Ernzerhof, *Phys. Rev. Lett.* **1996**, *77*, 3865-3868.

[14] aF. Weigend, M. Haser, H. Patzelt, R. Ahlrichs, *Chem. Phys. Lett.* **1998**, *294*, 143-152; bK. Eichkorn, F. Weigend, O. Treutler, R. Ahlrichs, *Theor. Chem. Acc.* **1997**, *97*, 119-124; cW. Kuchle, M. Dolg, H. Stoll, H. Preuss, *J. Chem. Phys.* **1994**, *100*, 7535-7542; dX. Y. Cao, M. Dolg, H. Stoll, *J. Chem. Phys.* **2003**, *118*, 487-496.

[15] S. Grimme, J. Antony, S. Ehrlich, H. Krieg, *J. Chem. Phys.* **2010**, *132*.

[16] K. Eichkorn, O. Treutler, H. Ohm, M. Haser, R. Ahlrichs, *Chem. Phys. Lett.* **1995**, *240*, 283-289.

[17] A. V. Marenich, S. V. Jerome, C. J. Cramer, D. G. Truhlar, *J. Chem. Theor. Comp.* **2012**, *8*, 527-541.

[18] T. Lu, F. W. Chen, *Acta Chim. Sin.* **2011**, *69*, 2393-2406.

[19] T. Lu, F. W. Chen, *J. Comp. Chem.* **2012**, *33*, 580-592.

[20] G. te Velde, F. M. Bickelhaupt, E. J. Baerends, C. F. Guerra, S. J. A. Van Gisbergen, J. G. Snijders, T. Ziegler, *J. Comp. Chem.* **2001**, *22*, 931-967.

[21] F. Aquilante, J. Autschbach, R. K. Carlson, L. F. Chibotaru, M. G. Delcey, L. De Vico, I. F. Galvan, N. Ferre, L. M. Frutos, L. Gagliardi, M. Garavelli, A. Giussani, C. E. Hoyer, G. Li Manni, H. Lischka, D. X. Ma, P. A. Malmqvist, T. Muller, A. Nenov, M. Olivucci, T. B. Pedersen, D. L. Peng, F. Plasser, B. Pritchard, M. Reiher, I. Rivalta, I. Schapiro, J. Segarra-Marti, M. Stenrup, D. G. Truhlar, L. Ungur, A. Valentini, S. Vancoillie, V. Veryazov, V. P. Vysotskiy, O. Weingart, F. Zapata, R. Lindh, *J. Comp. Chem.* **2016**, *37*, 506-541.

[22] aB. O. Roos, R. Lindh, P. A. Malmqvist, V. Veryazov, P. O. Widmark, *J. Phys. Chem. A* **2004**, *108*, 2851-2858; bB. O. Roos, R. Lindh, P. A. Malmqvist, V. Veryazov, P. O. Widmark, *Chem. Phys. Lett.* **2005**, *409*, 295-299.

[23] aM. Douglas, N. M. Kroll, *Ann. Phys.* **1974**, *82*, 89-155; bB. A. Hess, *Phys. Rev. A* **1986**, *33*, 3742-3748.

[24] aF. Aquilante, L. Gagliardi, T. B. Pedersen, R. Lindh, *J. Chem. Phys.* **2009**, *130*; bF. Aquilante, R. Lindh, T. B. Pedersen, *J. Chem. Phys.* **2008**, *129*; cF. Aquilante, P. A. Malmqvist, T. B. Pedersen, A. Ghosh, B. O. Roos, *J. Chem. Theor. Comp.* **2008**, *4*, 694-702; dF. Aquilante, T. B. Pedersen, R. Lindh, *J. Chem. Phys.* **2007**, *126*.

[25] aK. Pierloot, H. L. Zhao, S. Vancoillie, *Inorg. Chem.* **2010**, *49*, 10316-10329; bW. Wu, J. T. De Hont, R. Parveen, B. Vlaisavljevich, W. B. Tolman, *Inorg. Chem.* **2021**, *60*, 5217-5223.
[26] R. F. W. Bader, *Chem. Rev* **1991**, *91*, 893-928.